Hard and soft flutter of thin plates in laminar incompressible flows: weakly and strongly nonlinear analyses

Johann Moulin[1] † and Olivier Marquet[1]

[1]ONERA, Universiy Paris Saclay, Meudon, France.

(Received xx; revised xx; accepted xx)

We investigate numerically the role of incompressible flow nonlinearities on the periodic flutter of a thin plate mounted on a system of bending/torsion linear springs located at its center of mass. The steady flow solution gets unstable to linear flutter eigenmodes at a critical reduced velocity. Close to that threshold, limit cycle oscillations of the plate appear for lower and upper reduced velocity, depending on the nature of the bifurcation. A weakly nonlinear analysis is first developed to compute the coefficients of the cubic amplitude equations that determine the subcritical or supercritical nature of the bifurcation close to the threshold. A parametric investigation of the solid-to-fluid mass ratio and Reynolds number shows that the bifurcation is supercritical (soft flutter) at low Reynolds numbers $Re < 90$ independently of the mass ratio, and gets subcritical for intermediate Reynolds number $90 < Re < 2000$ and low mass ratio $\tilde{m} < 100$. For larger values of the Reynolds number $2000 < Re < Re_w$, that remains bounded by the critical Reynolds number for the onset of vortex-shedding, the bifurcation is subcritical (hard flutter) independently of the mass ratio. The bifurcation scenarii are further investigated at the Reynolds number $Re = 500$ with a Time Spectral Method allowing to compute accurately periodic solutions with large amplitude oscillations. The transition from a supercritical to a subcritical bifurcation when decreasing the mass ratio is thus scrutinized, thus revealing a double-fold bifurcation scenario at intermediate mass ratio. The bifurcation is supercritical, as shown by the weakly nonlinear analysis, but a fold bifurcation of limit cycle solutions occurs slightly above the critical reduced velocity, leading to (unstable) limit cycle oscillations at lower reduced velocity. The second fold of periodic solutions finally lead to the branch of large amplitude oscillations that are observed in time marching simulations. The double fold bifurcation is finally discussed in light of experimental results Amandolèse (2016).

1. Introduction

The flutter phenomenon is well understood as a linear instability in the sense that, above some critical velocity threshold, the coupled fluid-structure system possesses a pair of complex conjugate eigenvalues with a positive growth rate. These aspects were revisited in **??** with a particular focus on the role of fluid viscosity.

However, if the governing equations are nonlinear — and they are (should be), because Nature is —, the unbounded exponential growth predicted by linear theory is saturated at some point, leading to finite amplitude oscillations *via* a Hopf bifurcation. Depending on the nature of the nonlinearity at play, the flutter bifurcation may be of a supercritical or subcritical nature (often denominated respectively as "soft flutter" and "hard flutter"). For a supercritical bifurcation, linear analysis usually provides a conservative stability criteria since the LCO amplitude grows smoothly from the bifurcation point. In the subcritical case however, large amplitude stable solutions exist

† Email address for correspondence: johann.moulin@onera.fr

well below the linear threshold. Finite amplitude perturbations can then suddenly transition the system from a stable steady-state to a high-amplitude solution.

The occurrence of subcritical flutter was first reported by (Woolston *et al.* 1955, 1957) using a nonlinear pitching spring with cubic stiffness and freeplay and an indicial function approach for the incompressible aerodynamics. In particular they showed that a soft torsion spring† leads to flutter oscillations well below the linear threshold. In contrast a hard spring preserves a supercritical flutter. Numerous investigations on the role of nonlinear spring stiffness have confirmed and enriched those findings (e.g. (Lee & Jiang 1999) and references therein, or more recently (Padmanabhan *et al.* 2018)). The common hypothesis that a hard pitching spring leads to supercritical flutter was then nuanced by Coller & Chamara (2004) who exhibited some counter examples, using center manifold theory. In all above mentioned studies, the aerodynamics were modeled through variants of unsteady thin airfoil theory (Theodorsen 1935; Bisplinghoff *et al.* 1955) which is linear.

More recently, efforts to model nonlinear aerodynamics have been made. The ONERA stall model (Petot D 1989)‡ was used to take into account dynamic stall in the aeroelastic behavior of high-aspect ratio wings (Tang & Dowell 2002; Stanford & Beran 2013). In the transonic regime, (Schewe *et al.* 2003) showed experimental evidence of strong fluid nonlinear effects that limit the amplitude of flutter oscillation. In particular, coexisting flutter LCO's were found for a supercritical¶ NLR 7310 airfoil. The coexistence of these solutions was later reproduced with Euler-based numerical simulations and attributed to different dynamical behaviors of shocks on the upper and lower surface of the (asymmetrical) NLR 7310 airfoil (see §7.2 in the review by Bendiksen (2011)). Numerical investigations by (Thomas *et al.* 2002) reported both super- and subcritical bifurcations on a transonic symmetrical NACA64A010A airfoil, using Harmonic Balance solutions of the Euler equation. In (Van Rooij *et al.* 2017), parametric investigations of the flutter bifurcation of a supercritical NLR7301 airfoil in inviscid transonic flows were reported. In particular, the effect of the heaving-to-pitching natural frequency ratio was investigated. In (Thomas *et al.* 2004), evidence was provided on the role of viscosity in the transonic regime by comparing aeroelastic Harmonic Balance solutions of the Euler and RANS Spalart Allmaras models. In this work, viscosity tends to have a "hardening" effect, i.e. drives the bifurcation towards supercritical.

Turning now to the subsonic regime, nonlinear fluid effects on flutter have often been investigated in the context of airfoils pitching around a nonzero static angle of attack, close to the static stall angle (Razak *et al.* 2011; Bhat & Govardhan 2013; Menon & Mittal 2019). For airfoils at zero static angle of attack, nonlinear fluid effects were mostly investigated experimentally. In (Dimitriadis & Li 2009; Šidlof *et al.* 2016), the flutter of spring-mounted NACA0012 airfoil was investigated, whereas a similar study was conducted in (Amandolese *et al.* 2013), replacing the airfoil profile with a rigid flat plate. Both studies were performed at a moderate Reynolds, $Re \simeq 10^4$. Each time, hysteresis and subcritical LCO's were reported, showing that not only transonic nonlinearities can saturate the flutter oscillation growth. In addition, Amandolese *et al.* (2013) showed the co-existence of low- and high-amplitude LCO solutions in a range of post-critical flow velocities. By ensuring that the experimental set-up yielded an "as linear as possible" solid model, they suggested that nonlinear aerodynamic effects are the origin of the observed behavior. However, the exact nature of the physical phenomenon involved remains an open question. Finally, we note that due to the mostly experimental nature of these investigations, the effect of the governing non-dimensional parameters is not easy to grasp, as they are often varied

† A *soft spring* (resp. *hard spring*) is a spring with decreasing (resp. increasing) stiffness as deformation increases

‡ or (Dimitriadis 2017, §8.4.3) for a more recent presentation

¶ Here, supercritical has nothing to do with the nature of flutter, but refers to these airfoils shapes that delay the apparition of supersonic regions on the suction side.

simultaneously. For example, increasing the wind velocity increases the reduced velocity and the Reynolds number together. Knowing that the Reynolds number typically governs the amount of nonlinearity in the fluid model, a separate evaluation of its effect would nevertheless be valuable. Similarly the effect of solid-to-fluid mass ratio is rarely investigated alone despite its known major effect on the critical flutter frequency (see **??**), and hence, on the amount of fluid unsteady effects.

In this work, we aim at isolating and understanding the role of incompressible fluid nonlinearities on the flutter bifurcation of a spring-mounted heaving and pitching plate. To that aim we consider a purely linear solid model immersed in a two-dimensional Navier–Stokes flow. The chapter is organized as follows. In section 2, the physical model and computational approaches are briefly described. In section 3, the effect of mass ratio and Reynolds number on the type of flutter is investigated, using a weakly nonlinear approach. In addition, we take advantage of the weakly nonlinear formalism to exhibit a scalar field that quantifies how much the different regions of the flow contribute to the type of bifurcation. Finally, in section 5, the fully nonlinear regime is visited where radically different flow features are observed for supercritical and subcritical cases. In the process, a particularly interesting scenario is discovered, where two stable solutions coexist for a given reduced velocity. This scenario enlightens the experimental results of Amandolese *et al.* (2013).

2. Governing equations and numerical methods

We investigate the non-linear dynamics of a rigid plate mounted on heaving and pitching springs and immersed in a two-dimensional incompressible viscous flow. As discussed in section **??**, eight non-dimensional parameters defined in **??**, govern that fluid-structure interaction problem. As always in this thesis, five of them — the heaving-to-pitching frequency ratio $\mathbf{\Omega}$, the structural dampings ζ_h, ζ_p, the radius of gyration r_θ and the position of the elastic axis x_θ — are kept fixed to the values already specified in **??**. The parameters that vary in the present chapter are the solid-to-fluid mass ratio $\tilde{m} = m/(1/2\rho_f c^2)$, the Reynolds number $Re = \rho_f U_\infty c/\mu$ and the reduced velocity $U^* = U_\infty/(c\sqrt{K_\theta/I_{\text{ea}}})$

The dynamics of the spring-mounted plate is governed by two (damped) linear oscillator equations **??**, whereas the flow verifies the incompressible Navier–Stokes equations. This system of coupled equations, described in detail in **??**, is formally written here as the following first-order in time evolution equation

$$\mathscr{M}\frac{\partial \mathbf{q}}{\partial t} + \mathscr{R}(\mathbf{q}) = 0 \tag{2.1}$$

where the variable $\mathbf{q} = (h, \theta, u_h, u_\theta, \mathbf{U}, p, \mathbf{\Lambda})^{\mathrm{T}}$ gathers all variables necessary to describe the fluid-solid interaction. The first four scalar variables allow describing the dynamics of the rigid plate. They are the heaving h and pitching θ displacements, as well as the corresponding velocities u_h and u_θ. The incompressible flow is described with the velocity $\mathbf{U}$ and pressure p fields. Finally, the variable $\mathbf{\Lambda}$ defined at the fluid-solid interface represents the local stress exerted by the fluid onto the solid. The exact definition of the linear operator $\mathscr{M}$ in front of the time-derivative and of the nonlinear residual vector $\mathscr{R}$ are given in **??**. In this residual, the first four components corresponds to the two coupled damped harmonic oscillators, written as a first-order problem in time. The fifth and sixth component correspond to the Navier–Stokes momentum and mass conservation equations. The last equation corresponds to the equality of fluid and solid velocities at the fluid-solid interface. Again, we refer to **??** for more details.

Several (numerical) methods are used in the following to compute the unsteady nonlinear solutions that emerge close to the critical reduced velocity U_c^* where steady solutions of the above equation ($\mathscr{R}(\mathbf{q}) = 0$) get linearly unstable (see **??** for more detailed investigations on

the linear stability of the system). These nonlinear unsteady solutions often consist in time-periodic solutions, also referred to as Limit Cycle Oscillations (LCO), that can be computed using either classical time-marching method (see section 2.1) or nonlinear modals methods specifically developed to compute periodic solutions (see section 2.2). In this work, the following modal methods are used: the weakly-nonlinear analysis (WNL) introduced in details in **??** and the Time Spectral Method (TSM) presented in **??**. The weakly-nonlinear analysis is a semi-analytical method based on the assumption of weak nonlinear effects and is thus tends to be valid close to the critical reduced velocity U_c^*. It is mainly used in the following to determine the supercritical or subcritical nature of the flutter bifurcation. On the other hand, the Time Spectral Method allows computing nonlinear periodic solutions independently of their amplitude (strength of the nonlinearity). In both cases, those modals methods give access to unstable LCO, which can not be determined with a time-marching method, unless stabilization techniques are implemented (Jallas *et al.* 2017; Shaabani-Ardali *et al.* 2019).

2.1. *Time-marching simulations of nonlinear solutions*

A Backward Differences Formula of order two (BDF2) is used to approximate the time derivative:

$$\left.\frac{\partial \mathbf{q}}{\partial t}\right|(t_n) \simeq \frac{3\mathbf{q}(t_n) - 4\mathbf{q}(t_{n-1}) + \mathbf{q}(t_{n-2})}{2\Delta t} \tag{2.2}$$

yielding the following implicit nonlinear system at each timestep

$$\mathscr{M}\mathbf{q}(t_n) + \frac{2\Delta t}{3}\mathscr{R}(\mathbf{q}(t_n)) = \frac{4}{3}\mathbf{q}(t_{n-1}) - \frac{1}{3}\mathbf{q}(t_{n-2})$$

The latter is solved using the pressure segregation method proposed in Badia & Codina (2007) which consists in mixing a pressure correction approach (Guermond *et al.* 2006) to handle the incompressibility constraint with Dirichlet–Neumann fixed-point iterations for handling the fluid–structure coupling. Solving the implicit nonlinear system is thus decomposed in solving a sequence of simpler linear problems that are: (i) a linear advection-diffusion equation for the fluid velocity, (ii) a Poisson problem for the pressure increment and (iii) a four-by-four† linear (the solid dynamics are fully linear due to the elastic axis being at the center of mass) solid problem. The fluid problems are space-discretized using the well-known Taylor–Hood $(\mathbb{P}_2, \mathbb{P}_1)$ finite element pair for (velocity,pressure) *via* the finite element library FreeFEM (Hecht 2012). The discrete problems are solved in parallel with preconditioned Krylov subspace methods from the PETSc library (Balay *et al.* 2019), accessed through its FreeFEM interface. More details about the algorithm can be found in **??**.

2.2. *Methods for periodic nonlinear solutions*

We now describe the weakly-nonlinear analysis in §2.2.1 and the time spectral method in §2.2.2, that both allows to determine periodic nonlinear solutions. Compared to the time-marching simulations, these methods can be used to compute both stable and unstable Limit Cycle Oscillations.

2.2.1. *Weakly nonlinear analysis*

In the vicinity of the critical reduced velocity U_c^*, the amplitude of the LCO are expected to be small. That property can be used to approximate the periodic solution and thus to efficiently determine the supercritical or subcritical nature of the bifurcation. As detailed in **??**, the weakly nonlinear approximation is based on a development of the solution in the vicinity of the critical

† Recall the heaving and pitching velocities have been introduced to formulate the problem at first order in time...

velocity. The departure from the critical velocity is written

$$\frac{1}{U^{*2}} = \frac{1}{U_c^{*2}} + \epsilon^2 \Delta_{U^*} \tag{2.3}$$

with ϵ is a small positive parameter and the integer $\Delta_{U^*} = \pm 1$ is introduced to choose the departure side. According to the methods of multiple scales (Nayfeh & Balachandran 1995), the solution $\mathbf{q}$ is then searched in the form of a series of ϵ powers:

$$\mathbf{q} = \mathbf{q}_0 + \epsilon \underbrace{\left(\tilde{A} \widehat{\mathbf{q}}_c e^{\mathbf{i}\omega_c t} + \text{ c.c.} \right)}_{\mathbf{q}_1} + \epsilon^2 \mathbf{q}_2 + \epsilon^3 \mathbf{q}_3 + \dots \tag{2.4}$$

where $\mathbf{q}_0$ is solution of the steady-state equation **??** at the critical velocity U_c^* and the first-order solution $\mathbf{q}_1$ is proportional to the marginally stable eigenmode $\widehat{\mathbf{q}}_c$ oscillating at frequency ω_c. The small but finite-size complex amplitude $A = \epsilon \tilde{A}$ of this critical eigenmode is solution of the well-known Stuart–Landau equation:

$$\frac{\mathrm{d}A}{\mathrm{d}t} = \alpha \left(\frac{U_c^{*2}}{U^{*2}} - 1 \right) A + \beta |A|^2 A \tag{2.5}$$

where the complex coefficient α drives the linear term while the complex coefficient β drives the cubic nonlinear term. As explained in chapter **??**, this amplitude equation results from a compatibility condition obtained at third-order in (2.4), which gives the following definition of the linear α and nonlinear β ciefficients,

$$\alpha = -\frac{1}{U_c^{*2}} \frac{\left\langle \mathbf{q}_c^\dagger, \mathscr{L} \mathbf{q}_c \right\rangle}{\left\langle \mathbf{q}_c^\dagger, \mathscr{M} \widehat{\mathbf{q}}_c \right\rangle} \qquad \text{and} \qquad \beta = \frac{\left\langle \mathbf{q}_c^\dagger, \mathscr{F}_{\text{res}}(\widehat{\mathbf{q}}_c, \mathbf{q}_2{}^{|A|^2}, \mathbf{q}_2{}^{A^2}) \right\rangle}{\left\langle \mathbf{q}_c^\dagger, \mathscr{M} \widehat{\mathbf{q}}_c \right\rangle}. \tag{2.6}$$

The linear coefficient α only depends on the critical eigenmode $\mathbf{q}_c$ while the nonlinear coefficient β also depends on the second-order solution $\mathbf{q}_2$. Both coefficients depends on the critical adjoint eigenmode $\mathbf{q}_c^\dagger$. The exact definition of the scalar product $\langle \cdot, \cdot \rangle$, linear operators $\mathscr{L}$ and $\mathscr{M}$ and residual vector $\mathscr{F}_{\text{res}}$ is given in **??**.

Once these coefficients are determined, the dynamics of the Limit Cycle Oscillations is obtained by injecting the polar decomposition of the amplitude $A = Re^{\mathbf{i}\omega_{\text{nl}} t + \phi}$ in (2.5), yielding first that the real amplitude R satisfies

$$\frac{\mathrm{d}R}{\mathrm{d}t} = \mathfrak{Re}\,(\alpha) \left(\frac{U_c^{*2}}{U^{*2}} - 1 \right) R + \mathfrak{Re}\,(\beta) R^3 \tag{2.7}$$

Periodic solutions satisfying $dR/dt = 0$, we obtain either the trivial solution $R = 0$ (which gives the base flow solution $\mathbf{q}_0$) or non-zero amplitude solution

$$R^2 = \frac{\mathfrak{Re}\,(\alpha)}{\mathfrak{Re}\,(\beta)} \left(1 - \frac{U_c^{*2}}{U^{*2}} \right) \tag{2.8}$$

The existence of the LCO thus clearly depends on the sign of $\mathfrak{Re}\,(\alpha)/\mathfrak{Re}\,(\beta)$. It exists for flutter velocity above (resp. below) the critical value (resp. $U^* < U_c^*$) when $\mathfrak{Re}\,(\alpha)/\mathfrak{Re}\,(\beta) > 0$ (resp. $\mathfrak{Re}\,(\alpha)/\mathfrak{Re}\,(\beta) < 0$). To determine the supercritical of subcritical nature of the bifurcation, we also need to know the stability of the trivial solution $R = 0$, that is given by the sign of the linear term in (2.7). In the following, we will mainly consider the case where $\mathfrak{Re}\,(\alpha) < 0$, so that the trivial solution gets unstable for $U^* > U_c^*$. The bifurcation is then supercritical if $\mathfrak{Re}\,(\beta) < 0$, since

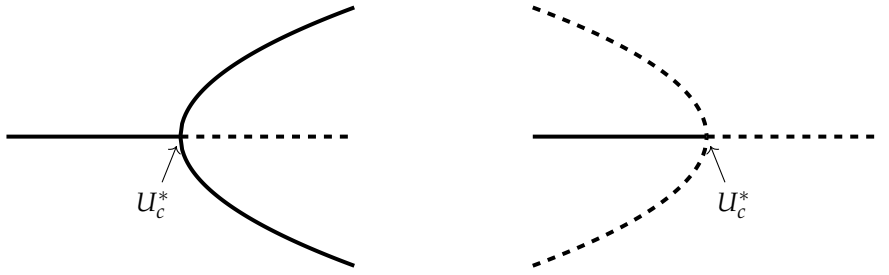

(a) Supercritical, $\tilde{\beta} > 0$ ($\mathfrak{Re}\,(\alpha) < 0, \mathfrak{Re}\,(\beta) < 0$)

(b) Subcritical, $\tilde{\beta} < 0$ ($\mathfrak{Re}\,(\alpha) < 0, \mathfrak{Re}\,(\beta) > 0$)

Figure 1: Nature of the bifurcation depending on the signs of $\mathfrak{Re}\,(\beta)$ and given $\mathfrak{Re}\,(\alpha) < 0$. The amplitude is represented as a function of U^*. The central horizontal branch always represents the trivial $R = 0$ solution that becomes unstable for $U^* > U_c^*$. By convention, the solid (resp. dashed) lines represent stable (resp. unstable) solutions.

the LCO solution then exists for $U^* > U_c^*$, while it is subcritical if $\mathfrak{Re}\,(\beta) > 0$. The frequency of the LCO $\omega = \omega_c + \omega_{nl}$ is the sum of the linear critical frequency ω_c and the non-linear correction ω_{nl} given by

$$\omega_{\mathrm{nl}} = \left(\mathfrak{Im}\,(\beta)\frac{\mathfrak{Re}\,(\alpha)}{\mathfrak{Re}\,(\beta)} - \mathfrak{Im}\,(\alpha)\right)\left(1 - \frac{U_c^{*2}}{U^{*2}}\right). \tag{2.9}$$

Knowing this frequency and the real amplitude R from (2.8), we can reconstruct analytically the first-order approximation for any components of the LCO. In particular, the temporal evolution of the pitching angle is given by

$$\theta(t) = 2\sqrt{\frac{1}{\tilde{\beta}}\left(1 - \frac{U_c^{*2}}{U^{*2}}\right)}\cos\left[(\omega_{\mathrm{c}} + \omega_{\mathrm{nl}})t + \phi + \phi_{\theta_c}\right] \tag{2.10}$$

where we have introduced the normalized quantity $\tilde{\beta}$

$$\tilde{\beta} = \frac{\mathfrak{Re}\,(\beta)}{\mathfrak{Re}\,(\alpha)|\widehat{\theta}_c|^2} \tag{2.11}$$

From eq. (2.10), the amplitude of the pitching motion is seen to depend only on $\tilde{\beta}$ and the deviation to the threshold given by the factor $1 - (U_c^*/U^*)^2$. As a consequence $\tilde{\beta}$ — its inverse, exactly — quantifies how fast the amplitude of the pitching oscillations grows when moving away from U_c^*. More precisely, a large positive $\tilde{\beta}$ corresponds to a supercritical bifurcation with slowly increasing amplitude whereas a very negative $\tilde{\beta}$ indicates a strongly subcritical bifurcation. When $\tilde{\beta} = 0$, the cubic nonlinear term in the amplitude equation (2.5) vanishes. This means that the nonlinearities at stake order ϵ^3 are not strong enough to saturate the linear growth of the flutter instability. In such cases, the weakly nonlinear analysis must typically be pushed at higher order. We chose not to pursue this path and simply note that results of the weakly nonlinear analysis around $\tilde{\beta} = 0$ should be interpreted with caution. To confirm them, we will rather consider the strongly nonlinear analysis developed below, in section 2.2.2.

Identifying the fluid and geometric nonlinearities The nature of the bifurcation is entirely driven by the scalar parameter $\tilde{\beta}$, defined in eq. (2.11). We now propose a decomposition of this parameter into two contributions that quantify the fluid and geometric nonlinearity.

Coming back to the definition (2.6) of the nonlinear coefficient β, the resonant forcing $\mathscr{F}_{\mathrm{res}}$

(exactly defined in **??**) is formally written as

$$\mathscr{F}_{\text{res}}(\widehat{\mathbf{q}}_{\text{c}}, \widehat{\mathbf{q}}_2^{|A|^2}, \widehat{\mathbf{q}}_2^{A^2}) = \left(0, 0, \mathscr{F}_{\text{res}}^{u_h}, 0, \mathscr{F}_{\text{res}}^{\mathbf{U}}, 0, \mathscr{F}_{\text{res}}^{\mathbf{\Lambda}}\right)^{\text{T}} \tag{2.12}$$

to highlight that it has non-zero components only for the heaving momentum equation (third component), the Navier–Stokes momentum equation (fifth) and the velocity continuity equation at the fluid-solid interface (seventh). The terms $\mathscr{F}_{\text{res}}^{u_h}$ and $\mathscr{F}_{\text{res}}^{\mathbf{\Lambda}}$ are due to the trigonometric nonlinearities inherent to the rotation movement of the plate. Indeed, in the heaving equation, the lift obtained in the rotating frame $(\mathbf{e_X}, \mathbf{e_Y})$ must be projected back onto the laboratory vertical axis $\mathbf{e_y}$ (*cf* **??**). In the interface boundary condition, it is the vertical velocity of the plate that must be projected back in the rotating axis (*cf* **??**). These terms thus correspond to the so-called *geometric nonlinearities*. On the contrary, the term $\mathscr{F}_{\text{res}}^{\mathbf{U}}$ is generated by *fluid nonlinearities* of the Navier–Stokes momentum equation which are the convection term, including the modification of the convective velocity by the domain's motion. Based on that decomposition of the resonant forcing, we can thus develop the nonlinear coefficient β as the sum

$$\beta = \beta_{\text{f}} + \beta_{\text{g}}$$

of the fluid β_{f} and geometric β_{f} contributions defined as

$$\beta_{\text{f}} = \int_{\Omega_{\text{f}}} f_{\beta_{\text{f}}}(\mathbf{X}) d\mathbf{\Omega} \quad \text{and} \quad \beta_{\text{g}} = \frac{\mathscr{F}_{\text{res}}^{u_h}\, {u_h}^{\dagger\star}}{\left\langle \mathbf{q}_{\text{c}}^{\dagger}, \mathscr{M}\widehat{\mathbf{q}}_{\text{c}} \right\rangle} + \int_{\Gamma_{\text{fs}}} \frac{\mathscr{F}_{\text{res}}^{\mathbf{\Lambda}} \cdot {\mathbf{\Lambda}}^{\dagger\star}}{\left\langle \mathbf{q}_{\text{c}}^{\dagger}, \mathscr{M}\widehat{\mathbf{q}}_{\text{c}} \right\rangle} d\Gamma \,.$$

The scalar field $f_{\beta_{\text{f}}}(\mathbf{X})$ in the definition of the fluid contribution is defined as

$$f_{\beta_{\text{f}}}(\mathbf{X}) = \frac{\mathbf{U}^{\dagger\star} \cdot \mathscr{F}_{\text{res}}^{\mathbf{U}}(\widehat{\mathbf{q}}_{\text{c}}, \mathbf{q}_2{}^{|A|^2}, \mathbf{q}_2{}^{A^2})}{\left\langle \mathbf{q}_{\text{c}}^{\dagger}, \mathscr{M}\widehat{\mathbf{q}}_{\text{c}} \right\rangle}$$

and will be used to determine flow regions where the nonlinearity is at play. This quantity can be assimilated to different local quantities previously introduced in the literature to assess the regions of the flow that are most decisive to linear instabilities. The so-called *wavemaker* (Huerre & Monkewitz 1990; Gianetti & Luchini 2007), for example, writes as the product of the local norms of the adjoint and direct modes. It quantifies the drift of an eigenvalue of the linear stability problem to a spatially localized feedback force. Closer to our expression of $f_{\beta_{\text{f}}}$, Marquet & Lesshafft (2015) have introduced a way of decomposing an eigenvalue of the (fluid) stability problem as the integral of a local quantity, called *endogeneity*, that writes $\mathbf{U}^{\dagger\star} \cdot (\mathscr{J}^{\mathbf{U}}\widehat{\mathbf{U}})$ with $\mathscr{J}^{\mathbf{U}}$ the Jacobian of the fluid problem (formulated here only with velocity, for simplicity). Both these approaches have been applied to the vortex shedding instability behind a circular cylinder in (see (Paladini *et al.* 2019) for a direct comparison) and evidenced the sensitive regions of the flow. In our study, it is the fluid contribution to the nonlinear coefficient β_{f} that is decomposed as the integral of a local quantity, $\tilde{f}_{\beta_{\text{f}}}$. The latter may thus been seen as a (weakly) nonlinear extension of the endogeneity concept, where the resonant forcing is projected onto the adjoint mode instead of the linear operator.

Obviously, the decompositions proposed above hold also for the normalized quantity $\tilde{\beta}$ that we use in the following instead of β, for reasons explained before. Specifically,

$$\tilde{\beta} = \tilde{\beta}_{\text{f}} + \tilde{\beta}_{\text{g}}\,, \qquad \tilde{\beta}_{\text{f}} = \frac{\mathfrak{Re}\,(\beta_{\text{f}})}{\mathfrak{Re}\,(\alpha)|\theta_c|^2} \quad \tilde{\beta}_{\text{g}} = \frac{\mathfrak{Re}\,(\beta_{\text{g}})}{\mathfrak{Re}\,(\alpha)|\theta_c|^2} \tag{2.13}$$

and

$$\tilde{\beta}_{\text{f}} = \int_{\Omega_{\text{f}}} \tilde{f}_{\beta_{\text{f}}}(\mathbf{x})\,, \qquad \tilde{f}_{\beta_{\text{f}}} = \frac{\mathfrak{Re}\,(f_{\beta_{\text{f}}})}{\mathfrak{Re}\,(\alpha)|\theta_c|^2} \tag{2.14}$$

2.2.2. *Time Spectral Method*

To investigate LCOs with large amplitudes, and in particular the hard flutter occurring via a subcritical bifurcation, we consider the Time Spectral Method (TSM), belonging to the family of harmonic balance methods, that is designed to compute periodic solutions. A short explanation is provided here, and the reader is referred to chapter **??** for a detailed derivation.

In the Time Spectral Method, a spectral approximation of the time derivative in eq. (2.1) is considered, i.e.

$$\left.\frac{\partial \mathbf{q}}{\partial t}\right|(t_n) \simeq \omega \sum_{k=0}^{2N_h} d_k \mathbf{q}(t_{n+k}) \tag{2.15}$$

where $\omega = 2\pi/T$ is the (unknown) frequency of the T-periodic solution, evaluated at the $2N_h + 1$ instants $t_n = n/(2N_h + 1)T$, $n = 0, ..., 2N_h$ discretizing the period, and the coefficients d_k are given by

$$d_k = \begin{cases} \dfrac{1}{2}(-1)^{k+1} \csc\left(\dfrac{\pi k}{2N_h + 1}\right) & \text{if } k \neq 0 \\ 0 & \text{if } k = 0 \end{cases} \tag{2.16}$$

Note that the index $n + k$ must be understood modulo $2N_h + 1$ due to periodicity. Compared to the second-order BDF formula, eq. (2.2) (used in time-marching simulations) that depends only on three consecutive time instants, the above time-spectral derivative depends on all $2N_h + 1$ instants. Using eq. (2.15), the time-dependent governing equations can be recast into a system of $2N_h + 1$ coupled time-independent equations that writes:

$$\omega \mathbf{D}\,\mathbf{Q} + \mathbf{R}(\mathbf{Q}) = 0 \tag{2.17}$$

where the solution and residual vector are

$$\mathbf{Q} = \begin{pmatrix} \mathbf{q}(t_0) \\ \vdots \\ \mathbf{q}(t_{2N_h}) \end{pmatrix} \text{ and } \mathbf{R}(\mathbf{Q}) = \begin{pmatrix} \mathscr{R}(\mathbf{q}(t_0)) \\ \vdots \\ \mathscr{R}(\mathbf{q}(t_{2N_h})) \end{pmatrix} \tag{2.18}$$

The time-spectral derivation matrix $\mathbf{D}$ is defined (*cf* **??**) from the the coefficients (2.16). As the LCO frequency ω is unknown, one additional scalar equation is required to close the system. This equation may be arbitrary chosen and we here impose that the pitching velocity is zero, $u_\theta = 0$, at instant $t = 0$. The time-spectral solutions thus satisfy the system of equation (2.17) augmented with one scalar constraint. Its total size is $(2N_h + 1) \times K + 1$ where K is the number of degrees of freedom used for the spatial discretization of $\mathbf{q}$. To obtain accurate solutions, the number of harmonics N_h (equivalently, the number of instants $2N_h + 1$) and the number of spatial degrees of freedom K may quickly grow. Efficient numerical methods are then required to obtain time-spectral solutions with adequate discretizations. To address this challenging task, a solver was proposed in chapter **??** based on the combination of a Newton–Krylov strategy with the so called "block-circulant" preconditioner. This numerical method has been used to obtain results shown in the next section.

2.3. *Cross-validation of numerical methods*

The implementation of the weakly-nonlinear and time-spectral methods are validated by comparison with results of the time-marching simulations performed at the mass ratio $\tilde{m} = 1000$ and the Reynolds number $Re = 500$.

The frequency and the maximal pitching angle are depicted in Figure fig. 2a and fig. 2b, respectively, as a function of the reduced velocity. The reference results, corresponding to time-marching simulations performed with about 1400 timesteps per period, are reported with black

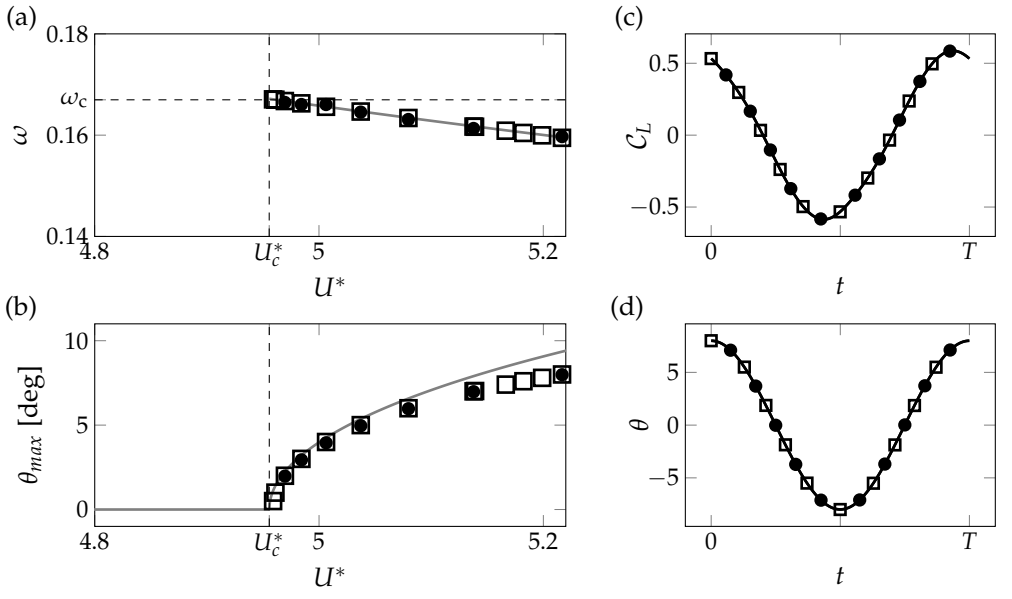

Figure 2: Comparison of numerical results obtained with time-marching simulations and modal methods for $\tilde{m} = 1000$ and $Re = 500$. The frequency (a) and the maximal pitching angle (b) of the LCO are presented as a function of reduced velocity for the weakly nonlinear analysis (gray solid line), the time spectral method ($N_h = 20$, squares) and the time-marching simulations (1400 timesteps per period, black dots). The vertical dashed line indicates the critical flutter velocity. Periodic evolution of (c) the lift coefficient and (d) the pitching angle are depicted for the time-spectral method and time-marching simulations (using the same symbols) for the reduced velocity $U^* = 5.22$.

dots in the figures. Results of the weakly-nonlinear analysis, shown with the grey curve, matches fairly well the time-marching results especially close to the critical reduced velocity. For the maximal value of the pitching angle (Figure fig. 2b), the disagreement clearly increases with the reduced velocity. Such a disagreement is expected and was already reported, for instance by (Gallaire *et al.* 2016) for the vortex shedding behind a circular cylinder. Interestingly, the frequency prediction is much better. Turning now to results of the time-spectral method with $N_h = 20$ (squares), they compare very well with time-marching results, for all values of the reduced velocity considered here. The critical flutter velocity U_c^* corresponds to that predicted by the linear stability analysis. In addition, the periodic evolution of the lift coefficient (Figure fig. 2c) and pitching amplitude (Figure fig. 2d) obtained with the time-spectral method and time-marching simulation also perfectly match. Similar agreements were obtained for other sets of parameters $(\tilde{m}, Re)$.

3. Hard and soft flutter with weakly nonlinear analysis

The first objective of this section is to understand the effect of the mass ratio and Reynolds number on the sub- or supercritical nature of flutter bifurcation, using the weakly nonlinear analysis (§3.1). Results of the decomposition approach, previously introduced in eq. (2.13), are then presented to quantify the distinct effect of the hydrodynamic and geometric nonlinearities on the bifurcation (§3.2).

Before addressing those objectives, we start by presenting a typical coupled-mode flutter LCO, obtained at $Re = 500$, $\tilde{m} = 1000$ and $U^* = 1.016U_c^*$. The solution is reconstructed in time (at second order) using eq. (2.4). In fig. 3a, the time signals for the heaving displacement (solid line)

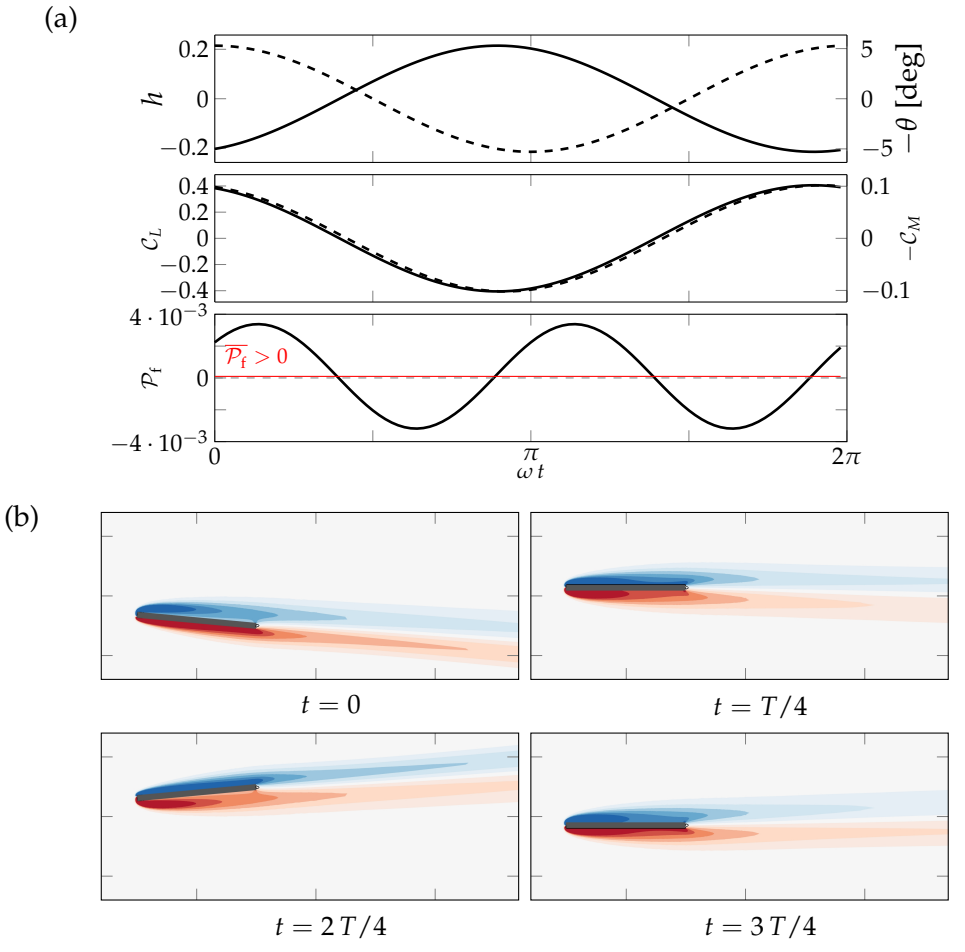

Figure 3: Weakly nonlinear flutter LCO at $Re = 500$, $\tilde{m} = 1000$ and $U^*/U_c^* = 1.016$. In (a) we present the time signals of the heaving displacement (solid) and pitching angle (dashed) (top part), the lift (solid) and moment (dashed) coefficients (central part) and the power transmitted by the fluid forces to the solid (bottom part). In (b), vorticity snapshots corresponding to four instants in the period are shown.

and pitching angle (dashed line) are purely sinusoidal. This is consistent with the signals obtained with TSM and time-marching computations using similar parameters in fig. 2. The heaving and pitching motion oscillate with a phase shift such that the pitching motion is "in advance" with respect to the heaving motion by slightly less than half a period. This phase shift is a typical feature of the coupled-mode flutter instability add reference. The lift (solid line) and moment (dashed line) coefficient signals, presented in the central part of fig. 3a, vibrate almost in phase with respect to each other, and with respect to the pitching angle shown above. Over one period of oscillation, this motion allows the extraction of a small, but positive, mean power from the flow to the solid (equal to the power dissipated by the structural damping). In fig. 3b, four snapshots of the vorticity field are presented. The flow features fully attached shear layers that evolve *quasi-steadily* in time, consistently with the low frequency $\omega \simeq 0.17$ of the flutter instability at the chosen set of parameters. One notice that in these snapshots, the wake seems to almost "rotate as a block" with the plate. Close to the plate, this is indeed the correct physical flow (as will be seen later in *cf* fig. 13). Far from the plate, this block-rotation becomes increasingly unphysical and is

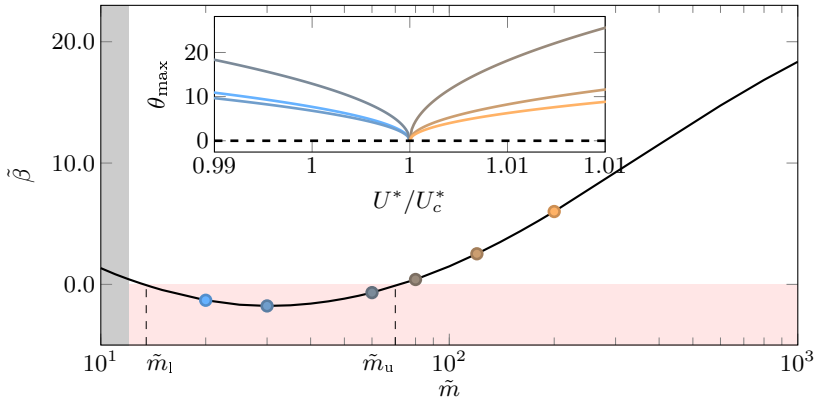

Figure 4: Nature of the flutter bifurcation at different mass ratio and constant $Re = 500$. The value of the criticality indicator $\tilde{\beta}$, built from weakly nonlinear analysis, is shown as a function of mass ratio. In the insert the amplitude of θ is represented as a function of U^*/U_c^* for the different mass ratio marked with solid symbols on the main curve ($\tilde{m} = 20, 30, 60, 80, 120, 200$). Note that we do not investigate the range $\tilde{m} < 12$ materialized by the gray area, since for those low mass ratio a static divergence mode is already unstable when the flutter threshold U_c^* is reached (cf **??**). This scenario is out of the validity assumptions of the present weakly nonlinear analysis.

entirely due to the *weakly nonlinear* nature of the method. This is not problematic however since the nature of the flutter bifurcation, that we explore in this section, is an asymptotic feature that is fully determined by the cubic coefficient of the normal form, eq. (2.5).

3.1. *Effects of mass ratio and Reynolds number on the bifurcation*

We first investigate the effect of the mass ratio on the bifurcation for the fixed Reynolds number $Re = 500$. For each mass ratio, the reduced velocity is varied to determine its critical value where the flutter instability occurs. The evolution of $\tilde{\beta}$, governing the supercritical or subcritical nature of the bifurcation and defined in eq. (2.11), is shown in fig. 4 when varying the mass ratio $\tilde{m}$. We recall that a solid heavier than the fluid corresponds tp $\tilde{m} > 1$. Three regions are observed in the figure. For high mass ratio $\tilde{m} > \tilde{m}_\mathrm{u}$, the bifurcation is supercritical ($\tilde{\beta} > 0$). For intermediate values in the range $\tilde{m}_\mathrm{l} < \tilde{m} < \tilde{m}_\mathrm{u}$, the bifurcation is subcritical ($\tilde{\beta} < 0$). And finally, for lower mass ratio $\tilde{m} < \tilde{m}_\mathrm{l}$, the bifurcation gets back to supercriticality. The transition values are $\tilde{m}_\mathrm{l} = 13.5$ and $\tilde{m}_\mathrm{u} = 70$ for the Reynolds number $Re = 500$ considered here. Note that those values should be considered with cautious, since they correspond to $\tilde{\beta} = 0$ for which the cubic amplitude equation (2.5) degenerates, as explained previously. To account for the nonlinear effect in that case, the quintic amplitude equation should be considered but this is out of the scope of the present paper. Instead, the effect of higher-order nonlinearities close to $\tilde{m}_\mathrm{u}$ will be investigated in §section 5 using time-spectral method or time-marching simulations. Note that the supercritical region at low mass ratio is of very small extension since it is bounded on its lower end by a region (grey in the figure) where divergence instability occurs for reduced velocity lower than the critical flutter velocity. The bifurcation diagrams corresponding to several values of $\tilde{m}$ are displayed in the insert of fig. 4. Since the critical reduced velocity varies with the mass ratio, we show the amplitude of θ as a function of the ratio between the reduced velocity and its critical value. The color of the different curves corresponds to the color of the solid circles in the main figure. As expected, the LCO branches exists above (resp. below) the threshold for supercritical (resp. subcritical) bifurcations displayed with orange (blue) colors. If the sign of $\tilde{\beta}$ gives the nature of the bifurcation, its absolute value $|\tilde{\beta}|$ indicates the strength of the nonlinearity and consequently the growth of the LCO amplitude when moving away from the threshold $U^* = U_c^*$.

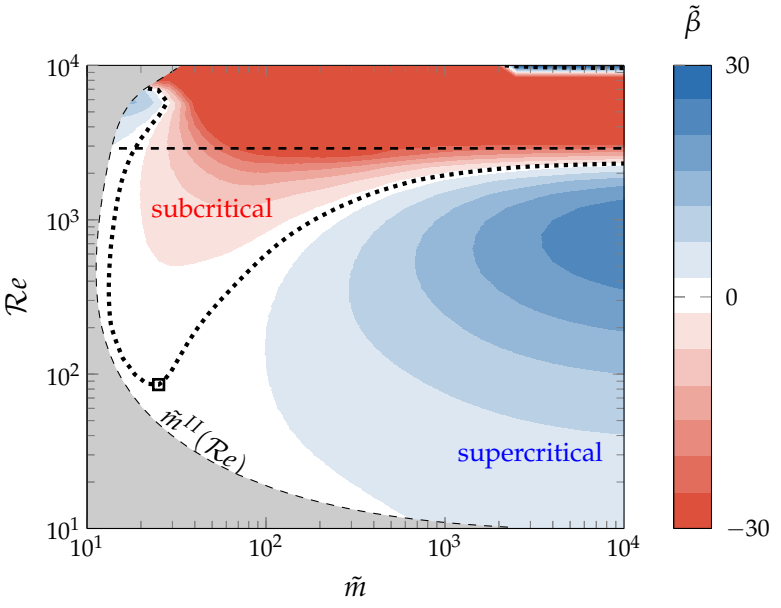

Figure 5: Effect of mass ratio and Reynolds number on the type of the flutter bifurcation. The colormap represents the criticality indicator $\tilde{\beta}$ in the $(\tilde{m}, Re)$ plane, whereas the dotted line indicates the contour $\tilde{\beta} = 0$ which separates subcritical and supercritical cases. The gray area on the left represents mass ratios $\tilde{m} < \tilde{m}^{II}(Re)$, for which a divergence is the primary instability (see **??**). The upper horizontal dashed line materializes the critical Reynolds $Re_{c,\text{wake}}$ above which the wake of the *fixed* plate becomes unstable.

This is clearly observed in fig. 4 by comparing the growth of the pitching amplitude when moving away from the threshold (inserted figure) with the corresponding values of $\tilde{\beta}$ (main figure). For large values of $|\tilde{\beta}|$ (blue or red colors), the maximal pitching amplitude of the LCO grows slowly. The nonlinear effects are strong compared to the linear growth and the saturation occurs for small amplitudes. On the other hand, for small values of $|\tilde{\beta}|$ (brown color), the maximal pitching amplitude of the LCO grows strongly close to the threshold. The nonlinearity being weak, the saturation occurs for larger amplitudes

By additionally varying the Reynolds number, we determine the transition between supercritical and subcritical bifurcations in the parameters space $(\tilde{m}, Re)$. Figure 5 displays the isocontours of $\tilde{\beta}$ in that parameters space, with positive values (in red) indicating a supercritical bifurcation and negative values (in blue) indicating a subcritical bifurcation. Johann, dans la figure, inverse les couleurs stp !. The black dotted curve highlights the transition between supercritical and subcritical regions. Supercritical bifurcations occurs predominantly for large mass ratio and low Reynolds number. For very low Reynolds number (for instance $Re = 20$), decreasing the mass ratio leads to the onset of the divergence instability occurring prior to the flutter instability. This region is marked grey and the dashed curve $\tilde{m}^{II}(Re)$ corresponds to codimension-two points where the flutter and divergence modes are both neutrally stable. For larger Reynolds number (around $Re = 10^2 - 10^3$), the bifurcation changes from supercritical and subcritical when decreasing the mass ratios. This is the scenario previously described for $Re = 500$, with a narrow supercritical region occuring for very low mass ratios, that are still larger than the divergence threshold. The critical Reynolds number for the onset of a subcritical bifurcation is $Re = \cdots$ (square in the figure). When increasing the Reynolds number, the lower critical mass-ratio $\tilde{m}_\text{l}$ slightly varies, unlike the upper critical mass ratio $\tilde{m}_\text{u}$ that strongly increases. Thus, for the Reynolds number

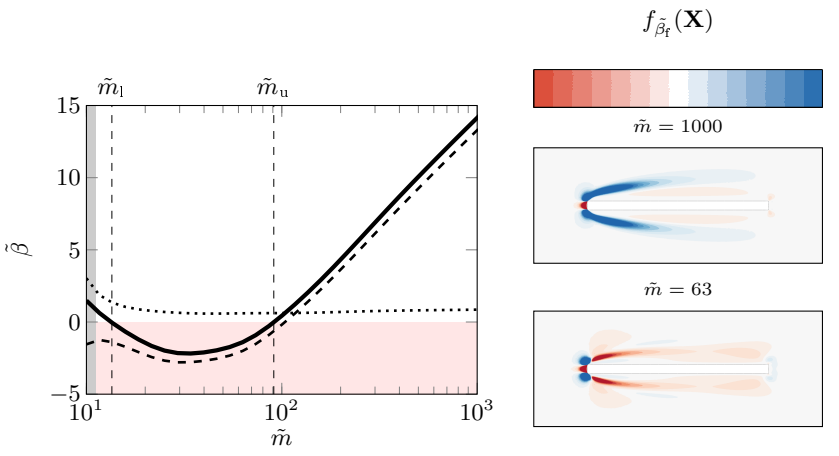

(a) (b)

Figure 6: Fluid and geometric nonlinearities. (a) Fluid $\tilde{\beta}_\mathrm{f}$ (dashed line) and geometric $\tilde{\beta}_\mathrm{g}$ (dotted line) contribution to the nonlinear coefficient $\tilde{\beta}$ (solid line) as a function of the mass ratio, (b) Spatial distribution of $\tilde{f}_{\beta_\mathrm{f}}(\mathbf{x})$ (its integral over the domain gives the value of the fluid contribution $\tilde{\beta}_\mathrm{f}$) for two values of the mass ratio corresponding to a supercritical bifurcation (top,$\tilde{m} = 1000$) and a subcritical bifurcation (bottom, $\tilde{m} = 63$). The Reynolds number is $Re = 540$.

$Re_{c,\mathrm{wake}} \simeq 2925$ (marked with the horizontal dashed line) corresponding to the onset of vortex-shedding instability (in the rigid case), the subcritical region extends up to the largest mass ratio shown in the figure. Interestingly, at these large mass ratios, the subcritical flutter instability occurs for lower Reynolds numbers than the vortex-shedding instability. For Reynolds number above $Re \longrightarrow Re_{c,\mathrm{wake}}$ (or $\tilde{m} \longrightarrow \infty$), results of the weakly analysis should be interpreted cautiously, since a vortex-shedding instability occurs in addition to the flutter instability. Still, we observe an abrupt transition from subcritical to supercritical for $Re \simeq 10^4$ and large mass ratio. This point is further discussed in §section 4.

3.2. *Fluid and geometric nonlinearities*

The model considered for the elastic motion of the rigid plate is purely linear. Still, the rotational motion of the plate induces a geometric nonlinearity in addition to the inherent fluid nonlinearity. The weakly-nonlinear analysis easily allows identifying those two contributions, as explained in §2.2.1 with the decomposition (2.13).

Figure 6a displays the evolution of the fluid $\tilde{\beta}_\mathrm{f}$ and geometric $\tilde{\beta}_\mathrm{g}$ contribution to the nonlinear coefficient $\tilde{\beta}$ as a function of the mass ratio for the fixed Reynolds number $Re = 540$. In that case, we recall that the bifurcation is supercritical for large ($\tilde{m} > \tilde{m}_\mathrm{u}$) and low ($\tilde{m} < \tilde{m}_\mathrm{l}$) values of the mass ratio, while it is subcritical for intermediate values ($\tilde{m}_\mathrm{l} < \tilde{m} < \tilde{m}_\mathrm{u}$). For all values of the mass ratio, the contribution of the geometric nonlinearity (dotted curve) is positive and, in most cases, it is small compared to the fluid contribution (dashed line), that evolves very similarly to the total contribution (solid line). In particular, the upper transition at $\tilde{m}_\mathrm{u}$ from a super- to sub-critical bifurcation is clearly driven by the fluid nonlinearity. On the other hand, around the lower transition at $\tilde{m}_\mathrm{l}$, the geometric and fluid nonlinearity have opposite contributions of equal strength. For small enough values of the mass ratio, the total contribution is even positive. Thus, the transition from sub-critical to super-critical bifurcation is driven by the geometric non-linearity at low mass ratios.

In cases where the bifurcation is driven by the fluid nonlinearity, we can determine the flow regions that mostly contribute by examining the spatial distribution of the scalar field $\tilde{f}_{\beta_\mathrm{f}}(\mathbf{X})$,

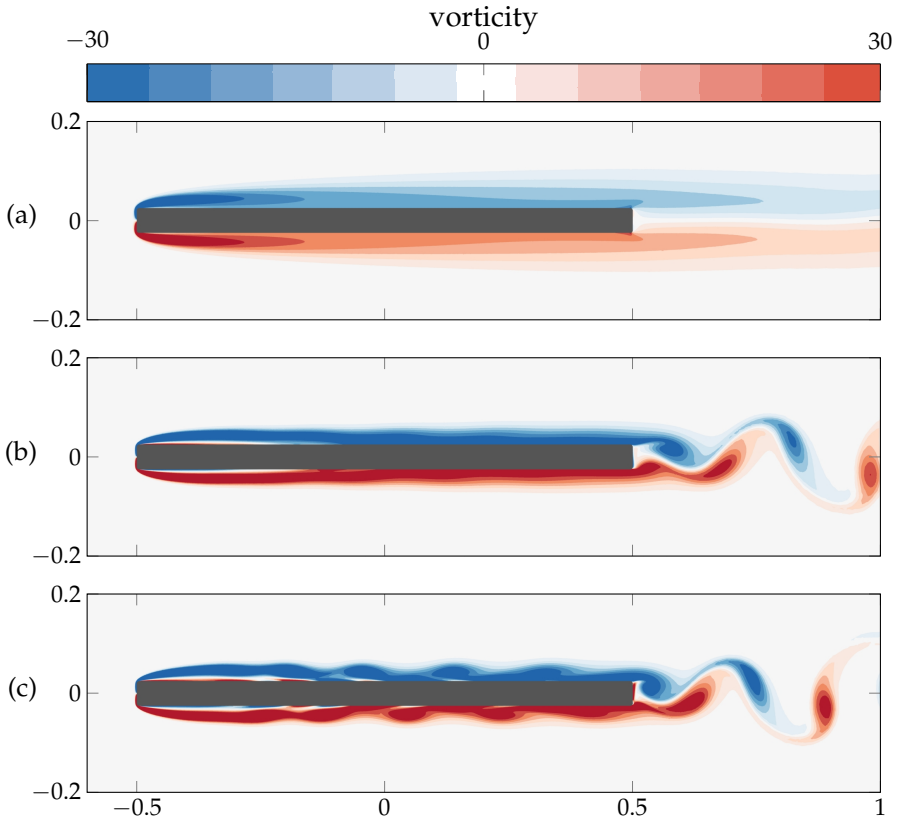

Figure 7: Instantaneous vorticity field around the *fixed plate* for (a) a steady solution at $Re = 2682$ and unsteady solutions at (b) $Re = 8325$ and (c) $Re = 10^4$.

defined in (2.14). Its integral over space gives the fluid contribution $\tilde{\beta}_\mathrm{f}$. Figure 6b displays $\tilde{f}_{\beta_\mathrm{f}}$ for two mass ratios corresponding to a supercritical bifurcation (top figure, $\tilde{m} = 1000$) and a subcritical bifurcation (bottom figure, $\tilde{m} = 63$). Largest values of $\tilde{f}_{\beta_\mathrm{f}}$ are obtained only close to the plate, and more specifically close to the leading-edge. For the largest mass ratio (top), the symmetric shear layers emerging from the leading-edge corners strongly contribute to the supercritical nature of the bifurcation. For the lowest mass ratio (bottom), this effect is (almost) entirely opposite and the bifurcation gets subcritical. The shear-layers around the leading-edge are thus the flow region responsible for the upper transition around $\tilde{m}_\mathrm{u}$

4. A mean flow approach for the bifurcation analysis at high Reynolds number and mass ratio

For the highest Reynolds numbers explored $Re \simeq 10^4$, the weakly nonlinear analysis predicts a brutal transition from subcritical to supercritical occuring for high mass ratio $\tilde{m} = 10^4$ (see fig. 5). After discussing the physical relevance of the linear and weakly nonlinear flutter analysis, an alternative mean flow-based approach is proposed and applied.

First, we recall that linear stability analysis predicts the destabilisation of a vortex-shedding mode for Reynolds number above $Re_{c,\mathrm{wake}} \simeq 2925$ (*cf* horizontal dashed line in fig. 5), with a frequency $\omega_\mathrm{wake} \simeq 11.2$ much higher than the flutter frequency. Therefore, the weakly nonlinear analysis developed around the base flow is questionable as the latter may not represent the

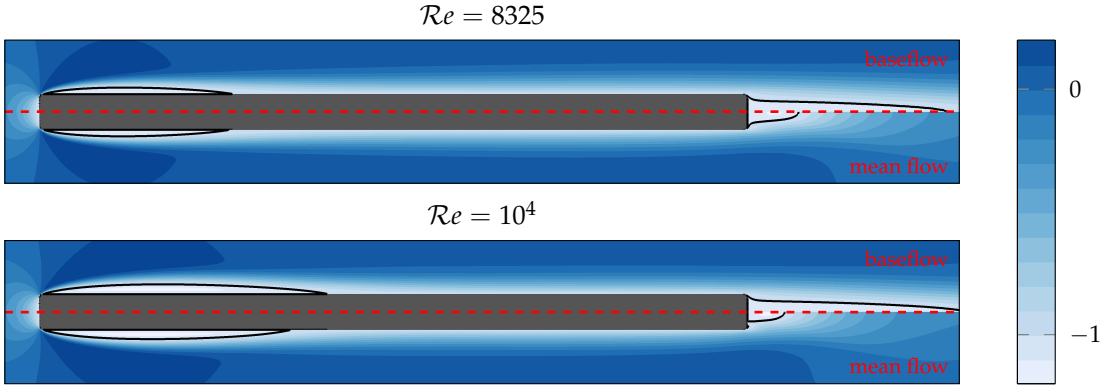

Figure 8: Spatial distribution of the streamwise velocity for the base (upper halves) and mean (lower halves) flow at Reynolds numbers $Re = 8325$ and $Re = 10^4$. The black curves delimit the recirculation regions.

physical flow seen by the plate. To better illustrate that discrepancy, two-dimensional direct numerical simulations of the flow around the fixed rigid plate (not mounted on two springs) have been performed for various Reynolds numbers. Snapshots of the vorticity fields are displayed in fig. 7. For $Re_{c,\mathrm{wake}} < Re \lesssim 8500$, the flow unsteadiness is mainly visible in the wake (see fig. 7-b)) with vortices of opposite signs that are alternatively shed at the trailing edge. The flow unsteadiness at the leading edge and around the plate is very weak and barely visible. For higher values of the Reynolds number, as $Re = 10^4$ corresponding to fig. 7(c), large fluctuations are clearly visible around the plate. More specifically, small vortices are shed from the leading-edge shear layers, travel downstream along the plate and interact with the trailing-edge vortices. For a thorough investigation of the interaction between those leading-edge and trailing-edge vortices when varying the plate's length, we refer to (Hourigan *et al.* 2001). Here, we focus on the effect of the flow unsteadiness on the (time-averaged) mean flow, that are shown and compared to the base flow in fig. 8. For $Re = 8325$ (top figure), the difference between the base (upper half) and mean (lower half) flows is large in the wake. The main effect of the fluctuations is to decrease the recirculation region at the trailing edge. The two symmetric recirculation regions located around the leading-edge corners are very similar in the base and mean flows. For $Re = 10^4$ (bottom figure), the stream-wise extent of the leading-edge recirculation regions clearly decreases in the mean flow.

In the following, we propose to take into account this mean-flow distortion in the nonlinear analysis of the flutter instability. Close to the critical Reynolds number $Re_{c,\mathrm{wake}}$ for vortex-shedding, a rigorous weakly nonlinear analysis may be performed around a critical set of parameters (mass ratio and Reynolds number) where the vortex-shedding and flutter modes get simultaneously unstable. This type of two-mode expansion was successfully applied, for example, by Meliga *et al.* (2012) for studying mode selection during vortex breakdown in swirling jets. Far from the critical Reynolds number, the two-mode weakly nonlinear analysis may not be accurate. Rather than focusing on this rigorous analysis, we propose a simpler alternative that replaces the base flow $\mathbf{q}_0$ by the hydrodynamic mean-flow $\overline{\mathbf{q}}$ in the weakly nonlinear expansion eq. (2.4). With this approach the weakly nonlinear analysis can be performed taking into account only the flutter mode, since all hydrodynamic modes of the meanflow are stable (see fig. 9). By doing so, we partially retain the nonlinear interaction between purely-hydrodynamic fluctuations and flutter instability, since the hydrodynamic mean-flow accounts for the nonlinear interaction of flow harmonics. However, we neglect the dynamic interaction between the purely-hydrodynamic harmonics and the flutter harmonics. That assumption is reasonable as the vortex-shedding

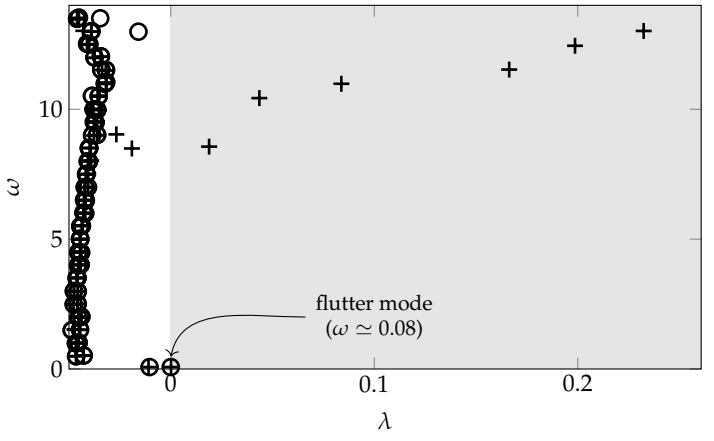

Figure 9: Comparison of the baseflow (crosses) and mean flow (circles) linear stability spectra at $Re = 10^4$, $\tilde{m} = 10^4$ and $U^* = 10.7$.

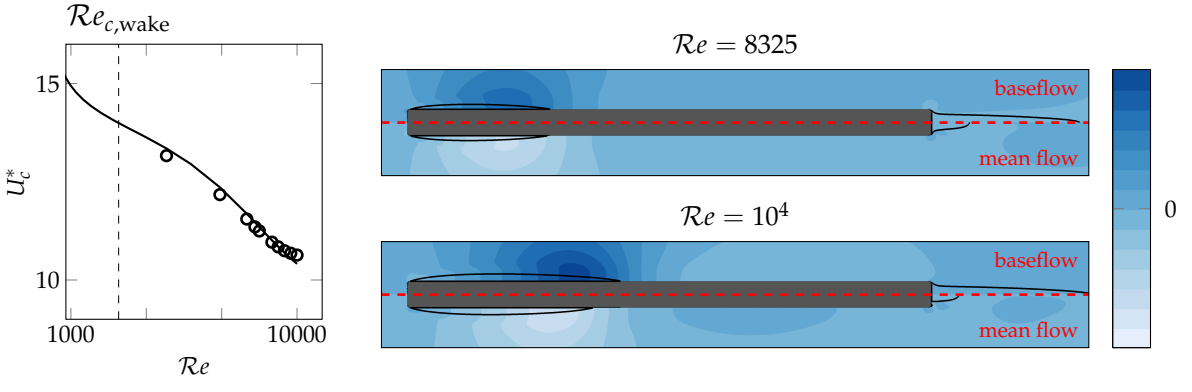

(a) (b)

Figure 10: Linear flutter analysis performed with the base and mean flows for $\tilde{m} = 10^4$. (a) Critical reduced velocity as a function of the Reynolds number obtained with base (solid line) and mean (circles) flow analyses. The critical Reynolds number $Re_{c,\mathrm{wake}}$ for the onset of vortex-shedding is depicted with the vertical dashed line. (b) Spatial distribution of the pressure field for the (real part of) flutter eigenmode obtained ar $Re = 8325$ and $Re = 10^4$ using the base flow (upper halves) and the mean flow (lower halves). Black curves delimit the recirculation regions in the base and mean flows.

frequency ($\omega_{\mathrm{wake}} = 11.2$ at $Re_{c,\mathrm{wake}}$) is much higher than the flutter frequency ($\omega \simeq 0.1$ for $\tilde{m} = 10^4$). In other words, the hydrodynamic vortex-shedding is time-averaged at the slow time scale of the flutter phenomenon. In the weakly nonlinear analysis around the mean flow, we thus analyze the nonlinear behavior of the low-frequency flutter instability that develops on the mean hydrodynamic flow

Let us first examine results of the linear flutter analysis of a plate of mass ratio $\tilde{m} = 10^4$. Figure 10(a) shows the critical reduced velocity as a function of the Reynolds number obtained with the base (solid curve) and mean (circles) flow analyses. They are very similar in both analyses, for all values of the Reynolds number. The marginally stable flutter modes obtained for the Reynolds numbers $Re = 8325$ and $Re = 10^4$ are shown in fig. 10(b) using the real part of the pressure fields. In both analyses and at both Reynolds numbers, they display larger values and gradients around the reattachement of the leading-edge recirculation regions. At $Re = 8325$, the baseflow and mean

flow modes are very similar in the leading-edge region. This is in agreement with the similar velocity threshold reported in 10(a). For $Re = 10^4$, the baseflow and mean flow modes are still qualitatively similar, but the latter is slightly shifted upstream, consistently with the shortening of the leading-edge recirculation region in the mean flow. This shift however appears to have only a small effect on the critical velocity shown in 10(a).

Let us now consider results of the weakly nonlinear analysis by examining more specifically the nonlinear coefficient $\tilde{\beta}$ defined in 2.11 and related to the strength of the cubic nonlinear term in the amplitude equation. Figure 11(a) displays that quantity, computed with the base (solid line) and mean (circles) flow, as a function of the Reynolds number. Results for the base flow indicate that, when increasing the Reynolds number up to $Re \approx 8500$, the bifurcation is more and more subcritical since $\tilde{\beta}$ is more and more negative. Above that Reynolds number, $\tilde{\beta}$ abruptly increases until it gets positive. For $Re = 10^4$, the weakly nonlinear analysis of the base flows thus predicts a supercritical bifurcation. This is the behaviour already observed in fig. 5 for high Reynolds numbers and mass ratios. Results for the mean flow are very similar up to $Re \approx 7000 - 8000$. Above $Re = 8000$, the mean flow results start to deviate from the baseflow analysis, but keep the same trend. The difference becomes striking for Re above ~ 9500 where the bifurcation remains subcritical in the mean flow analysis whereas it becomes brutally supercritical in the baseflow analysis. To further understand that behaviour, we display in 11(b) the spatial distribution of $\tilde{f}_{\beta_\mathrm{f}}$ whose integral over the computational domain is almost † equal to $\tilde{\beta}$. The upper plot displays the scalar field obtained with the base (upper) and mean (lower) flow at $Re = 8325$. In both cases, largest values are localized in the shear layer of the leading-edge recirculation regions. As noticed previously, the flow unsteadiness in those regions is very weak for that Reynolds number, and the mean flow is very similar to the base flow. This explains that $\tilde{\beta}$ are almost equal for the base and mean flow analyses. The wake of the plate, where the base and mean flow are very different, does not contribute at all to $\tilde{\beta}$ which explains why the shortening of the recirculation bubble in the mean flow does not impact $\tilde{\beta}$. The lower plot in 11(b) displays $\tilde{f}_{\beta_\mathrm{f}}$ for $Re = 10^4$. In this case, the mean flow distribution is clearly shifted upstream in comparison to the baseflow and the variations of $\tilde{f}_{\beta_\mathrm{f}}$ are less important than in the baseflow analysis. Overall, we note that the large impact of the mean flow on the value of $\tilde{\beta}$ is only due to mild differences in the balance between the supercritical (blue lobes) and subcritical (red lobes) regions. In the end, the proposed mean flow-based weakly nonlinear analysis shows that the type of the flutter bifurcation is strongly impacted by switching from baseflow to mean flow analysis for Re higher than ≈ 8000. This is linked to the fact that for such Reynolds numbers, unsteadiness occurs close to the leading edge and changes the topology of the leading edge shear layers, which are the most contributing regions to $\tilde{\beta}$. On the contrary, vortex shedding in the trailing edge area does not affect $\tilde{\beta}$. In any case, the present analysis, is not meant as a rigorous analysis, but rather as a way of stressing that results in fig. 5 must be taken with caution for high Reynolds numbers. In addition, it underlines again the critical role of the leading edge shear layers in deciding the type of the flutter bifurcation, and hence the need for accurate fluid modeling.

5. **Bifurcation scenarii at low Reynolds number $Re = 500$**

In this section, we focus on the bifurcation scenarii occurring at the low Reynolds number $Re = 500$ when varying the mass ratio and the reduced velocity. As seen in fig. 5, for that Reynolds number, the weakly nonlinear analysis predicts a transition from a supercritical bifurcation at high mass ratio ($\tilde{m} \sim 1000$) to a subcritical bifurcation at lower mass ratio ($\tilde{m} \sim 60$). We further explore those bifurcation scenarri using, in addition to the weakly nonlinear analysis valid close

† It was checked that geometric part $\tilde{\beta}_\mathrm{g}$ almost does not contribute to $\tilde{\beta}$ for the chosen mass ratio ($\tilde{m} = 10^4$).

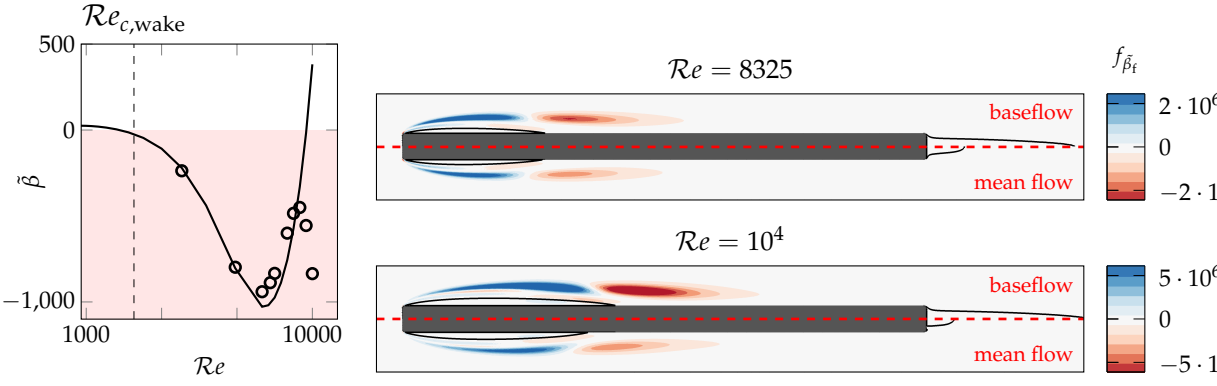

(a) (b)

Figure 11: Weakly nonlinear flutter analysis performed around the base or mean flows for $\tilde{m} = 10^4$. (a) Nonlinear coefficient $\tilde{\beta}$ as a function of the Reynolds number obtained with the base (solid line) and mean (circles) flow analyses. Negative and positive values correspond to subcritical and supercritical bifurcation, respectively. (b) Spatial distribution of the nonlinear fluid contribution $\tilde{f}_{\tilde{\beta}_f}$, (*cf* eq. (2.14)) is presented for both the base and mean flow analyses at $Re = 8325$ and $Re = 10^4$. The integral of that contribution gives the dominant contribution to $\tilde{\beta}$.

to the critical reduced velocities, the time spectral method (TSM) and time-marching simulations. The supercritical and subcritical bifurcation scenarii are described in §5.1 and §5.2, respectively. The more complex scenario obtained for intermediate mass ratio (when the nonlinear coefficient of the amplitude equation is close to zero) is examined in §5.3 and is discussed in light of experimental results by Amandolese *et al.* (2013).

we shall evaluate the stability of the LCO, *a posterori*. In this work, we merely estimate the LCO stability by restarting a standard time-integration computation from the TSM solution: if the time-integration stays on the LCO then we consider it stable, if not, we consider it unstable. This procedure is not a mathematically rigorous assessment of LCO linear stability and would be advantageously replaced by a Floquet multipliers computation.

5.1. *Supercritical bifurcation at high mass ratio*

Diagrams corresponding to a supercritical bifurcation are displayed in fig. 12 for the mass ratio $\tilde{m} = 1000$. The maximal pitching angle is shown as a function of the reduced velocity in fig. 12(a) where the solid curve and black dots correspond to results of TSM (with $2N_h + 1 = 41$ instants) and time-marching simulations (with about 1400 timesteps per period), respectively. The thin gray lines, materializing the weakly nonlinear results, are superimposed for comparison. For all reduced velocities, TSM and time-marching simulations superimpose perfectly so that we can not only conclude that TSM is accurate enough with this number of instants, but also that the LCO solutions are stable. The solution amplitude smoothly increases when increasing the reduced velocity above U_c^*. The maximum pitching angles is about 8° at $U^*/U_c^* = 1.05$. This is a relatively low amplitude, in comparison with those achieved for subcritical bifurcations, presented in the following. A consequence of these low amplitudes is that the weakly nonlinear approach (thin gray line) yields satisfying pitching amplitude predictions up to, say, $U^* = 1.05U_c^*$. In fig. 12(b), we show the bifurcation diagram for the oscillation frequency. On the considered interval of reduced velocity, the frequency only slightly decreases, in fact following a $1/U^*$ trend, which is the typical magnitude of the natural solid modes. In particular, we remark that the weakly

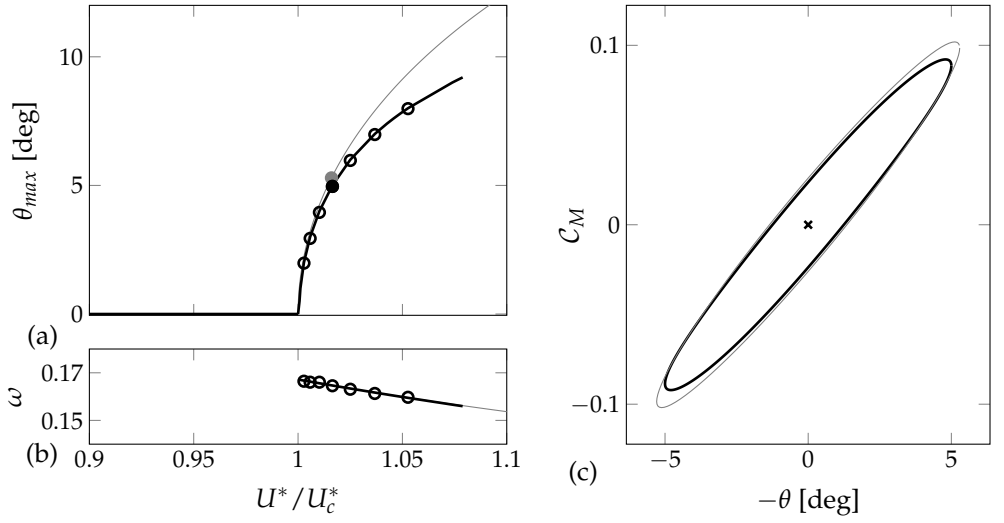

Figure 12: Supercritical bifurcation for $\tilde{m} = 1000$ and $Re = 500$. (a) Maximal pitching angle and (b) angular frequency as a function of the reduced velocity ratio U^*/U_c^* (with $U_c^* = 4.95$). (c) Phase diagram of the periodic solution $U^*/U_c^* = 1.016$ in the map (θ, C_M). The black and grey lines correspond to a branch of solutions obtained with time spectral and weakly nonlinear methods, respectively, while black circles correspond to results of time-marching simulations. The cross in (c) is the steady solution.

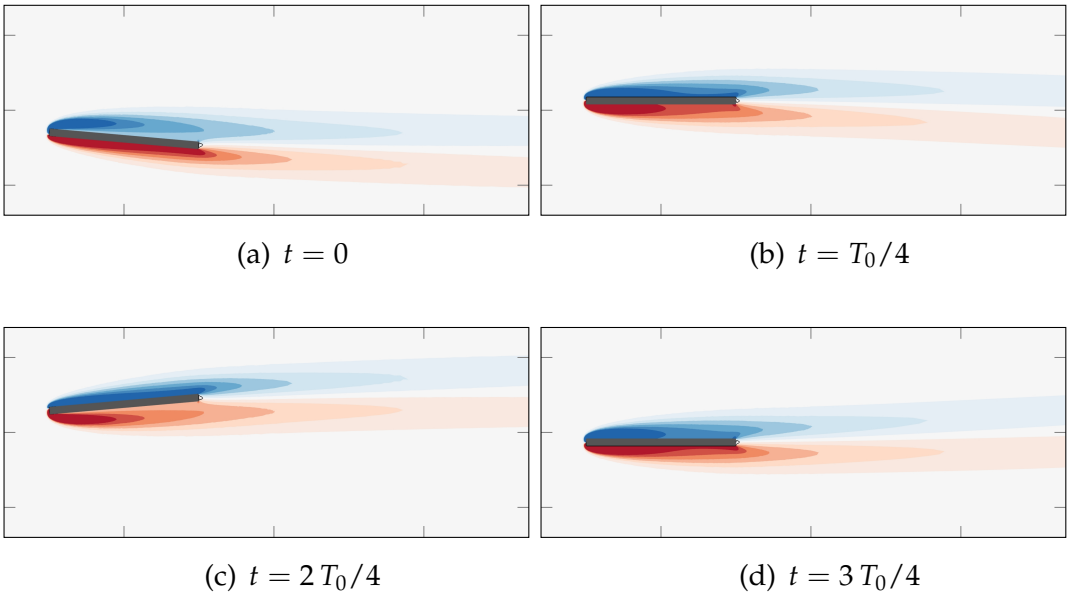

Figure 13: Supercritical bifurcation. Snapshots of vorticity for the low-amplitude LCO at $\tilde{m} = 1000$ and $U^*/U_c^* = 1.016$.

nonlinear analysis (thin gray line) perfectly captures the frequency evolution. For a given reduced velocity, $U^*/U_c^* = 1.016$ (filled circles in (a)), the solution obtained with TSM (solid black line) is represented in in fig. 12(c), in the $\theta - C_M$ map. The elliptic shape of the obtained orbit shows that both the plate displacement and moment coefficient follow a mostly harmonic evolution.

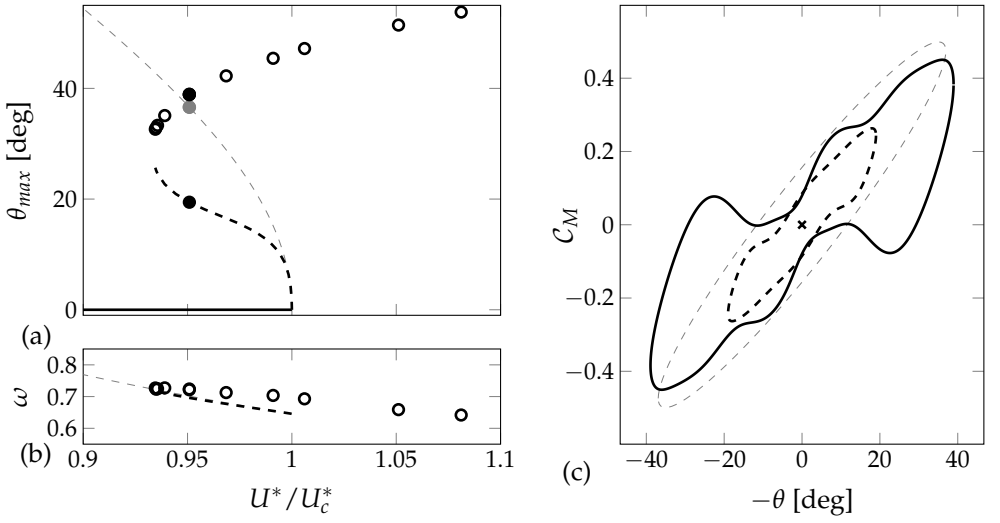

Figure 14: Subcritical bifurcation for $\tilde{m} = 60$ and $Re = 500$. Same legend as in fig. 12. The critical reduced velocity is $U_c^* = 1.33$. The dashed curves corresponds to unstable LCO. The LCO displayed in (c) corresponds to $U^* = 0.95U_c^*$.

The spatial distribution of the vorticity is depicted in fig. 13 at four instants of the period. At all instants, the flow remains attached to the plate and closely resembles the weakly nonlinear solution already shown in fig. 3. This further confirms the mildly nonlinear nature of this LCO. Furthermore, the flow also resembles the steady solution (see **??**), which is in agreement with the low-frequency $\omega \simeq 0.17$ characterizing this supercritical LCO. In other words, this LCO is a mildly nonlinear quasi-steady periodic solution.

5.2. *Subcritical bifurcation at low mass ratio*

We now consider the lower mass-ratio $\tilde{m} = 60$ for which the weakly-nonlinear analysis predicts a subcritical bifurcation (see triangle symbol in fig. 5). The bifurcation and phase diagrams are displayed in fig. 14 as for the supercritical bifurcation presented above. At the critical reduced velocity ($U^* = U_c^*$), an unstable LCO branch emerges and progresses towards lower reduced velocities with increasing amplitude. The branch predicted by the weakly-nonlinear analysis (dashed grey curve) is clearly of too high amplitude compared to the branch obtained with the TSM (dashed black line), showing that strong nonlinear effects are at plat, that can be only captured with the latter method. As the reduced velocity is further decreased, the amplitude of the pitching angle drastically increases when getting close to $U^* \simeq 0.93U_c^*$. This is observed for the TSM branch but not for the weakly-nonlinear branch. In fact, the weakly nonlinear analysis cannot approximate the turning point observed at $U^* \simeq 0.93U_c^*$, unless considering high-order terms in the expansion eq. (2.4), so as to obtain a quintic amplitude equation. When the branch turns and folds back with increasing U^*, the pitching amplitude increases drastically in a small range of reduced velocity. For the reduced velocity $U^* = 0.95U_c^*$, two solutions coexist: a low-amplitude LCO of maximal pitching angle $\theta_{max} = 20°$ and a high-amplitude LCO of maximal pitching angle $\theta_{max} \sim 40°$. Note that the nonlinearity is so strong that we could not compute the high-amplitude LCO branch using the TSM method, because the performance of the block-circulant preconditioner deteriorates too much for very large fluctuations, as explained in **??**. Still it is successfully used to capture the unstable branch of periodic solution that cannot be obtained with time-marching simulations, while the latter are reserved for computing the high-amplitude branch

of solutions (marked with black symbols), that are stable and still periodic. For the largest reduced velocity considered here ($U^* \simeq 1.08 U_c^*$), the maximal pitching angle is very large, around 60°. Contrary to the pitching amplitude, the oscillation frequency, shown in fig. 14(b), does not vary significantly. The large-amplitude branch possesses a slightly higher frequency than the unstable low-amplitude branch, but the global trend is, as in the supercritical case, dictated by the natural solid frequencies (not shown).

The unstable and stable LCO solutions co-existing at $U^*/U_c^* = 0.95$ are displayed in fig. 14(c) in the $\theta - C_M$ map, with dashed and solid lines, respectively. The central cross materializes the steady (stable here) solution and the thin gray dashed line the weakly nonlinear prediction. In contrast to the supercritical case (see fig. 12-c), both LCO orbits are far from ellipses. In particular, the large amplitude stable LCO (solid line) presents multiple local maxima of the moment coefficient. When the reduced velocity is decreased, the two solutions get closer and closer, until they collide and disappear for $U^* < 0.95$. This is a saddle-node bifurcation of periodic orbits.

Snapshots of vorticity are shown in fig. 15 for the (a) unstable low-amplitude and (b) stable high-amplitude solutions. In comparison with the periodic solution shown in fig. 13 for the supercritical bifurcation, the flow unsteadiness is stronger in both cases. For the low-amplitude solution in fig. 15(a), weak leading-edge vortices of opposite signs are alternatively formed in the shear layers on the plate's suction side, when the extremal values of the pitching angle are reached at $t = 0$ and $t = T/2$. These leading-edge vortices are then shed in the wake during the upstroke and downstroke phases, respectively. This vortex-shedding was not observed for the lower amplitude solution of the supercritical bifurcation since the shear-layers evolve quasi-steadily in this case. For the high-amplitude solution shown in fig. 15(b), the vortex-shedding pattern is more complex. First, we note that the vorticity field satisfies the spatio-temporal symmetry $\omega_z(x, -y, t + T/2) = -\omega_z(x, y, t)$ *i.e.* the pattern of the vorticity fields during the first and second half-periods are symmetric and of opposite sign. Thus, we can focus on describing only the first half-period.

At $t = 0$, the plate is at maximal pitching angle. A large recirculation region, delimited by the thin black line on the figure, (almost) covers the plate. A strong clockwise-oriented (blue) leading edge vortex is being fed by the detached upper leading-edge shear layer. In addition, an elongated counter-rotating (red) vorticity layer occupies the plate's upper surface. At $t = T/8$, the leading-edge vortex detaches from the feeding shear layer. Due to its large size, its centroid is already located above the plate's trailing edge. Concomitantly, a weaker secondary clock-wise leading-edge vortex is growing in the upper shear layer. Under the influence of the primary vortex, the counter-rotating upper side shear layer progressively detaches from the plate's surface. At $t = 2T/8$, the primary vortex has been shed in the wake, whereas the secondary vortex detaches from the feeding shear layer. In addition, the counter-rotating upper side shear layer has evolved into a better defined weak counter-rotating vortex. At $t = 3T/8$, the primary clockwise vortex has paired together with the weak counter-rotating vortex in the wake, forming a dipole. The secondary clockwise vortex is also shed in the wake so that the flow is fully re-attached on the upper side of the plate. Notice also the detached flow on the lower side of the plate which constitutes the early stage of the sequence of events in the lower shear layer symmetric to the one we are currently describing in the upper shear layer. At the plate's trailing edge, a tertiary weak clockwise vortex is being formed due the nose-down pitching motion of the plate that induces an upstream movement of the trailing edge. At $t = T/2$, this tertiary clockwise vortex appears more clearly as it is shed in the wake. For completeness, we can even guess a quaternary (very weak) clockwise vortex being formed at the trailing edge, and later released in the wake at $t = 5T/8$.

In order to get more detailed insights into the role of the different vortical structures generated during the high-amplitude LCO presented in fig. 15b, we propose in fig. 16 a more detailed description of the generation of the three dominant structures of that solution — *i.e.* the primary and secondary clockwise vortices and the counter-rotating vortex — and their connection to lift

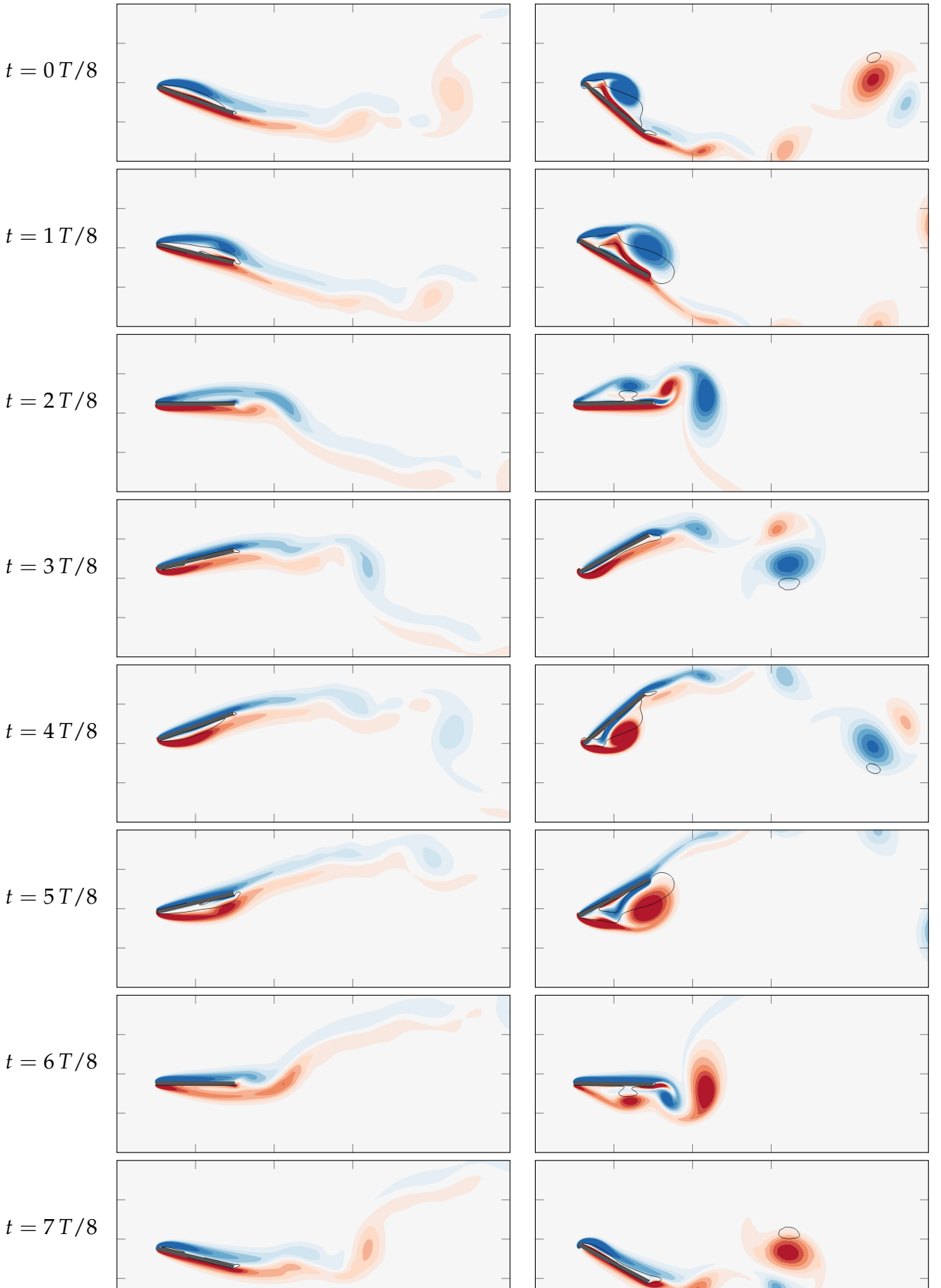
$t = 0\,T/8$
$t = 1\,T/8$
$t = 2\,T/8$
$t = 3\,T/8$
$t = 4\,T/8$
$t = 5\,T/8$
$t = 6\,T/8$
$t = 7\,T/8$

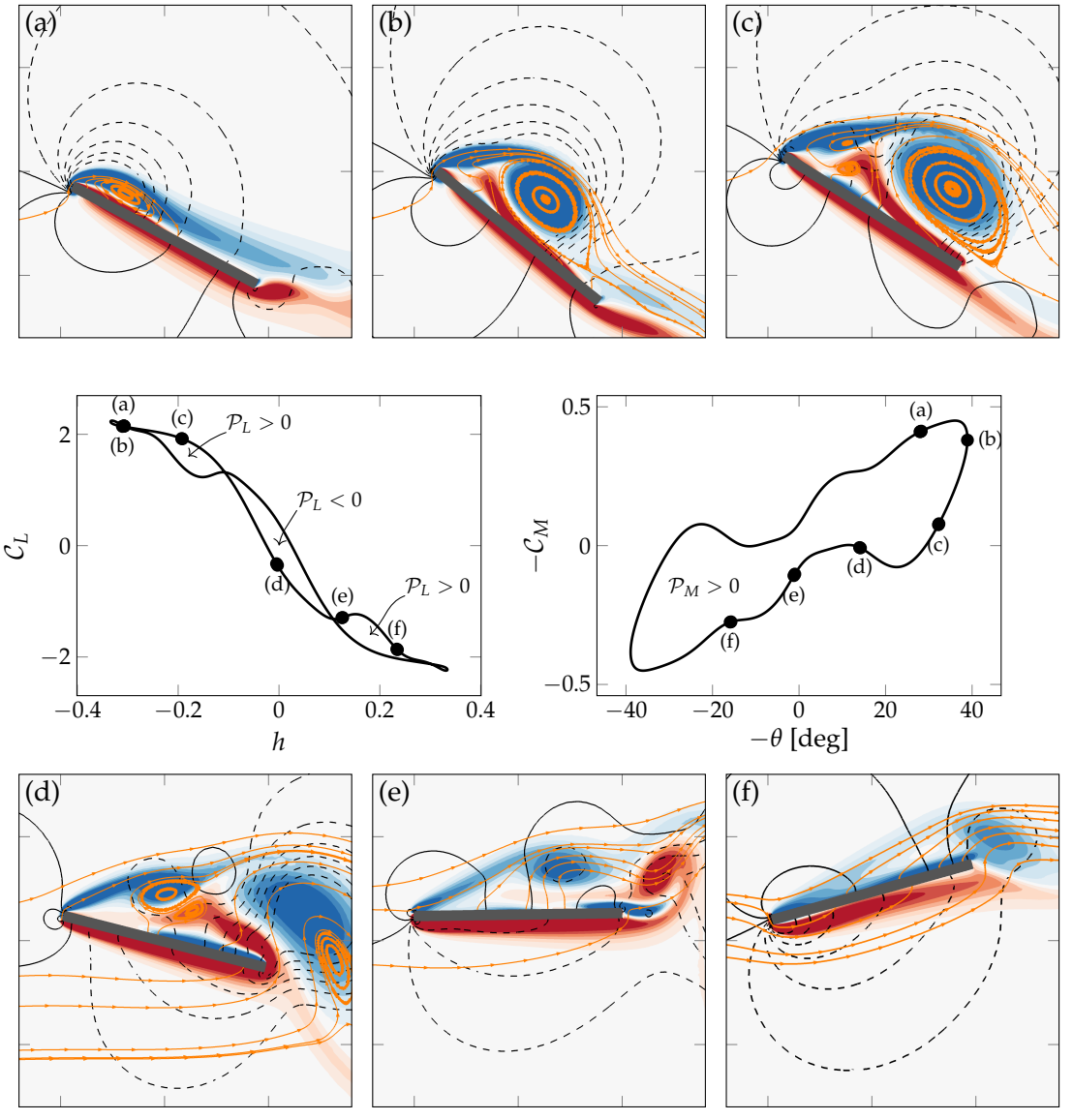

Figure 16: Description of the high-lift generation process of the high-amplitude stable solution in subcritical flutter ($\tilde{m} = 60$, $U^*/U_c^* = 0.95$). For each instant from (a) to (f), the vorticity (colored contours) and pressure (black isolines, negative values are dashed) fields are presented, along with a few streamlines in orange.

and moment forces. The LCO solution is presented in the $h - C_L$ and $\theta - C_M$ maps in the center of the figure. On a side node, we notice that, contrary to the $\theta - C_M$ orbit which is composed of one clockwise oriented loop, the $h - C_L$ orbit presents a more complex pattern of five loops (the three larger are well visible in the figure, the two small ones are found at the extremities of the orbit). Because these loops have opposite orientations, the average power provided by the fluid to the solid over one period along the heaving direction is negligible (by three orders of magnitude) with respect to the work along the pitching direction. Resuming now the description

of the vortical structures and their connection the aerodynamic forces, six points marked by letters from (a) to (f) are chosen on the orbit and the corresponding snapshots are presented in fig. 16. For comparison with fig. 15b, the vorticity field is represented, together with the pressure isocontours (black lines, negative contours with dashed line) and some streamlines (orange). Starting at point (a), we are just before the instant of maximum pitching angle. The upper leading edge shear layer is progressively detaching, thus creating a recirculation region down to the midchord. The low-pressure area at the leading edge induces a lift and strongly clockwise moment (recall the moment is computed at the elastic axis, which is the midchord). At (b), the primary clockwise vortex introduced before has formed and locates approximately above the midchord. The low-pressure area is still on the upper side of the plate, thus conserving a high lift. Despite it has displaced downstream with the vortex, the existence of a leading-egde high-pressure area on the lower side of the plate (due to incoming flow) still generates a strong clockwise moment. In (c), the primary vortex and the corresponding low-pressure area are above the trailing edge. A high-lift is still obtained but the moment brutally drops. Besides, the secondary clockwise vortex and the counter-rotating vortex are clearly visible at the leading edge. Between (c) and (d), the lift drops to negative values due to the upper side low-pressure area leaving the plate with the primary vortex. In the same interval of time, the moment slightly mitigates its drop thanks to the low-pressure leading edge regions associated to the secondary vortices. In (e) and (f), the lift and moment continue decreasing (*i.e.* anti-clockwise for the moment) due to all upper side low-pressure areas having left the surface of the plate, with the secondary vortices.

Overall, the previous descriptions of the supercritical (fig. 13) and subcritical (fig. 15(b) and 16) show that the super and sub-critical stable solutions are linked to radically different flows. In the supercritical case, the quasi-steady shear layers remain attached to the plate accross the cycle, whereas in the subcritical case, leading edge shear layers dynamically roll-up into a series of vortices of various strength and sign that generate strongly nonlinear lift and moment coefficients. We mention that this crucial importance of the shear layers was announced already in the analysis of the spatial decomposition of $\tilde{\beta}_\mathrm{f}$ proposed in section 3.2 where these regions where shown to decide the type of the bifurcation.

5.3. *Double-fold bifurcation scenario at intermediate mass ratio*

For intermediate mass ratio, there exists a transition between a supercritical and a subcritical bifurcation, that is identified, in the weakly nonlinear analysis, when the nonlinear coefficient vanishes, i.e. $\tilde{\beta} = 0$. However, results of the weakly nonlinear analysis are then of limited interest since, at third-order, all nonlinear terms vanish. Rather than considering the effect of higher-order terms in the development, we again use time spectral and time-marching simulations to investigate the nonlinear saturation of the LCOs at those intermediate mass ratio.

As for the previous bifurcation scenarii, we display the maximal pitching amplitude and frequency as a function of the reduced velocity in fig. 17(a) and (b), respectively. At the critical reduced velocity U_c^*, the bifurcation is supercritical in agreement with the weakly nonlinear prediction (grey curve) giving birth to a branch of stable low-amplitude LCO's. The amplitude growth away from U_c^* is very quick as the solution already reaches about 10° when the reduced velocity only exceeds U_c^* of less than one percent. This is the consequence of the small positive value of $\tilde{\beta}$ for this set of parameter (see fig. 4). On this branch, the solution is mostly harmonic as shown by the corresponding elliptic orbit in fig. 17c (inner solid line orbit). The vorticity field (not shown) is similar to fig. 13 despite the higher oscillation frequency, $\omega \sim 0.5$, shown in (b). Then, instead of the expected smooth increase of the LCO amplitude with increasing U^* away from the threshold, a first fold bifurcation is observed for $U^*/U_c^* \simeq 1.007$, leading to an unstable medium amplitude LCO branch. Traveling further along the medium amplitude branch, a second fold point is guessed, but as for the case $\tilde{m} = 60$, could not be reached with TSM for numerical reasons. Beyond the second fold, a high-amplitude stable branch of LCO's is retrieved

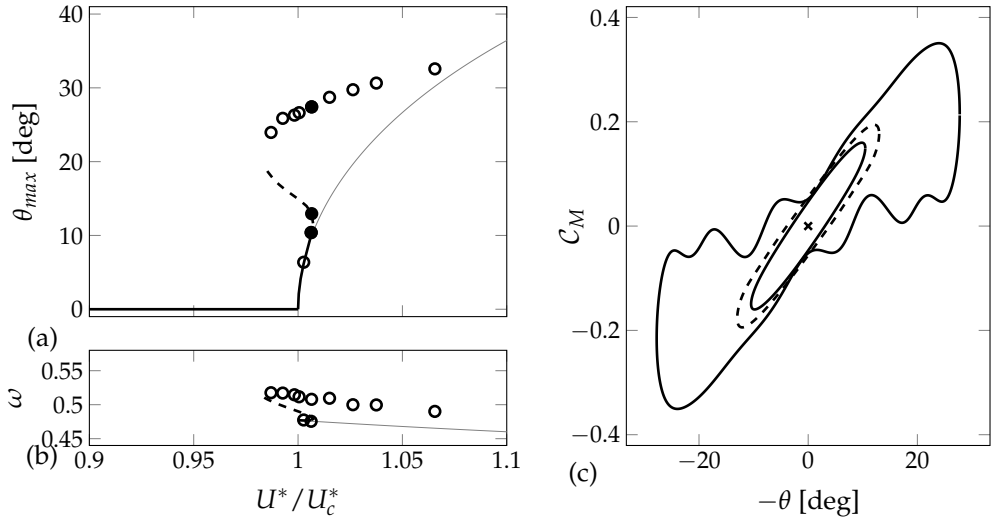

Figure 17: Bifurcation for intermediate mass ratio $\tilde{m} = 120$ ($Re = 500$). Same legend as in fig. 12. The critical reduced velocity is $U_c^* = 1.78$. The three LCO displayed in (c) corresponds to $U^*/U_c^* = 1.006$.

using DNS. On this branch, the solutions resembles fig. 15(b). On the range of reduced velocities between U_c^* and $1.007U_c^*$, the system possesses three nested LCO solutions, as shown in fig. 17c for $U^* = 1.006U_c^*$. The small and large amplitude LCO's are stable (solid lines) whereas the medium amplitude LCO is unstable (dashed line).

As a consequence, the case $\tilde{m} = 120$ gives rise to a non-standard bifurcation scenario where a supercritical Hopf is followed by two folds. Two important remarks then need to be made. First, because the second turning point is located for $U^* < U_c^*$, stable high-amplitude periodic solutions exist below the linear velocity threshold, despite the supercritical nature of the primary bifurcation. Second, if we suppose the system to be on the low amplitude branch, then, as one increases U^*, a brutal change of the system response will be observed around $U^*/U_c^* \simeq 1.007$, when the low amplitude branch disappears at the first fold, and the system consequently jumps to the large amplitude branch. In addition, if one now decreases U^* from the high amplitude branch, an hysteretic behavior is expected, as the system will go back to the steady baseflow solution only for $U^*/U_c^* < 0.98$ (where the second fold point is located), instead of $U^*/U_c^* = 1$.

We conclude this section by proposing in fig. 18 a synthetic view of the three different bifurcation scenarii observed before at $Re = 500$. In this figure, we gather the results for $\tilde{m} = 60$, 120 and 1000 previously shown in fig. 14, 17 and 12, respectively. The evolution of the pitching angle and oscillation frequency as a function of reduced velocity are reproduced, together with an additional representation of the heaving amplitude. The horizontal axis represents the ratio of U^* to U_c^* so that all bifurcations conveniently start at the same point. However, it should be kept in mind that the critical reduced velocities for these three mass ratios are different (from $U_c^* = 1.33$ at $\tilde{m} = 60$ to $U_c^* = 4.95$ at $\tilde{m} = 1000$). The pitching amplitude plot (a) is meant as a summary and the reader is reported to the figures corresponding to the individual mass ratios for a complete description. For the heaving amplitude (not shown until now), the notice that varying the mass ratio does not affect much the heaving amplitude: for example, at $U^* = 1.05U_c^*$, the heaving amplitude simply goes from about 0.3 at $\tilde{m} = 1000$ and $\tilde{m} = 120$ to 0.4 at $\tilde{m} = 60$. In comparison, the pitching amplitude goes from 10° to about 60°. This induces the idea that the difference between the high-amplitude subcritical LCO's and the low-amplitude supercritical LCO's is mainly in the pitching motion. Finally, in (c) we first observe that for all mass ratios,

[[Image Discarded Due To '/tikz/external/mode=list and make']]

Figure 18: Transition from subcritical to supercritical bifurcations at low Reynolds number ($Re = 500$) when increasing the mass ratio ($\tilde{m} = 60$ in blue, $\tilde{m} = 120$ in grey and $\tilde{m} = 1000$ in orange). (a) Maximal pitching angle, (b) maximal heaving displacement and (c) frequency of the LCO as a function of U^*/U_c^*. Dots and curves correspond to results of time-marching and time-spectral methods, respectively, while solid and dashed curves distinguish stable from unstable LCOs. In (c), the natural heaving and pitching frequencies are represented by dotted and dash-dotted curves, respectively.

	c/e	x_θ	Ω	ζ_h	ζ_p	r_θ
exp. (Amandolese *et al.* 2013)	23	0.08	0.78	0.002	0.015	0.35
present work	20	0	0.8	0	0.05	0.29

Table 1: Comparison of the parameters of the plate used by (Amandolese *et al.* 2013) with the present work.

the frequency evolves along a $1/U^*$ trend imposed by the natural solid frequencies that are materialized by the thin dotted (heaving) and dash-dotted (pitching) lines. The low-amplitude solutions at the highest mass ratios ($\tilde{m} = 1000$, orange) are rather associated to the heaving frequency, whereas the high-amplitude solutions at lower mass ratios shift towards the pitching frequency. Overall, the occurrence of large amplitude LCO's (and subcritical flutter) is associated with an increase of the oscillation frequency. It can be interpreted that high enough frequencies are necessary to generate the highly unsteady vortex shedding pattern associated to the large amplitude LCO's (see fig. 15b).

5.4. *Experimental evidence of the double-fold scenario*

In (Amandolese *et al.* 2013), the flutter response of a system similar to the one used in this work was investigated experimentally, in a wind tunnel. In particular, the assumption of a fully linear solid model that is used throughout the present work, was verified, at least for angles of attack lower than 25°. The characteristics of their spring-mounted plate, summarized in table 1, are similar to ours though not identical. In this paragraph we aim at comparing the bifurcation diagram obtained by these authors with the present work. If fitting our solid parameters to the experimental ones would have been possible, our 2D Navier–Stokes fluid model is not reliable at Reynolds as high as the one used experimentally ($1 \cdot 10^4 \leqslant Re \leqslant 3 \cdot 10^4$). Therefore, the following comparison is only qualitative.

By varying the wind velocity, the authors obtained the bifurcation diagrams that are reproduced in fig. 19a. High-amplitude subcritical responses and strong hysteresis, similar to the results of fig. 14 were observed. If those features are compatible with a classical subcritical Hopf scenario, the presence of the low amplitude response for $U^*/U_c^* \simeq 1.08$, marked by a red disk, remained unexplained by the authors. In fig. 19b, the bifurcation diagram for $(\tilde{m}, Re) = (120, 500)$ is reproduced. To ease the comparison with fig. 19a, a red disk symbol is added on the low-amplitude branch. By comparing the pitching (left) and heaving (right) amplitude diagrams, we see that the major difference between the low-amplitude and the high-amplitude branches is in the pitching dynamics. Indeed, whereas the pitching amplitude is almost tripled at $U^*/U_c^* \simeq 1.007$ when going from the low-amplitude to the high-amplitude branch, the heaving amplitude only increases of about 40%. These qualitative features are present in both the experimental results and in our numerical example. As a consequence, it can be argued that the supercritical Hopf bifurcation followed by two folds offers a possible explanation for the experimentally observed co-existence of (stable) low-amplitude supercritical and large-amplitude subcritical solutions.

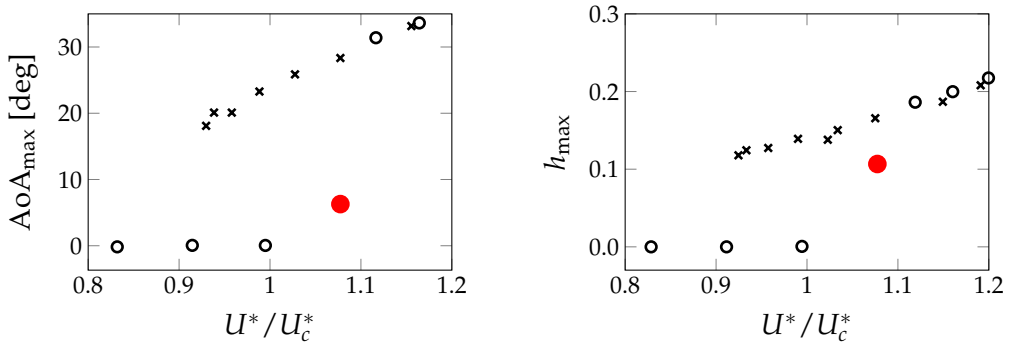

(a) Experimental results

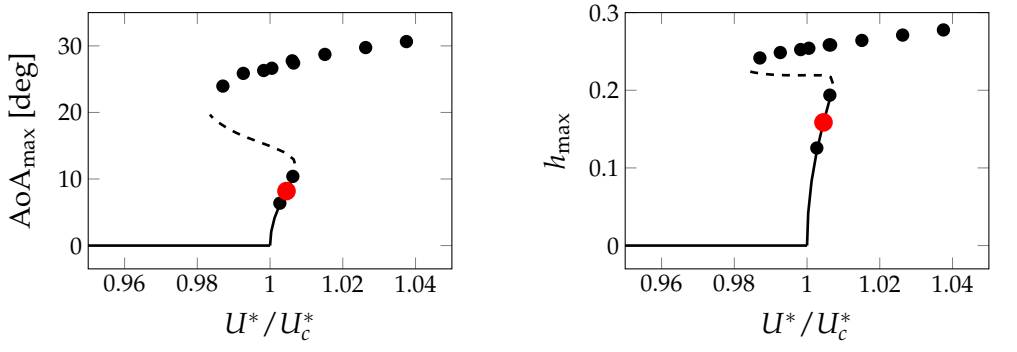

(b) Present numerical results

Figure 19: Qualitative comparison of the supercritical double-fold scenario exposed in fig. 18 with wind-tunnel data from (Amandolese *et al.* 2013). Pitching (left) and heaving (right) amplitude results are given for (a) the experimental results ($\tilde{m} = 2100$, $Re \simeq 30000$) and (b) the present numerical results ($\tilde{m} = 120$, $Re = 500$). For the description of (a), see fig. 18. In (b), circles (resp. crosses) mark increasing (resp. decreasing) wind velocity.

6. Conclusion

TO DO !

A. Grid convergence study

The sensitivity of the weakly nonlinear results with respect to computational domain size and grid refinement are presented in fig. 20a, for a subcritical case ($\tilde{m} = 1000, Re = 2682.81$). In the first column, the radius of the computational domain R is reported. In the second column, the interpolation error for the mesh adaptation process (*cf* **??**) is given whereas the corresponding number of triangles is reported in the third column. The last three columns present respectively the critical flutter velocity, the critical frequency and the normalized quantity $\tilde{\beta}$ defined in eq. (2.11). From the first to the fourth row, the computational mesh is refined. It is observed that the linear quantities,U_c^* and ω_c, are both almost converged already with the coarsest mesh. On the contrary, $\tilde{\beta}$ converges slowlier with the grid. This is easily linked to the small scale variations of its spatial distribution, as illustrated in fig. 11(b).

In the last three rows, the dependence of the results as a function of the computational domain size is explored. It is seen again that the linear quantities are very robust, while $\tilde{\beta}$ more significantly depends on R. With the smallest domain, $R = 10$, the obtained $\tilde{\beta}$ deviates about 7% from the

R	err	n_{tri}	U_c^*	ω_c	$\tilde{\beta}$
20	$3 \cdot 10^{-2}$	16,662	4.576	0.1808	−18.94
20	$1 \cdot 10^{-2}$	36,750	4.576	0.1809	−19.17
20	$5 \cdot 10^{-3}$	65,434	4.575	0.1809	−19.18
20	$3 \cdot 10^{-3}$	100,362	4.575	0.1809	−19.18
10	$1 \cdot 10^{-2}$	33,444	4.530	0.1828	−20.93
30	$1 \cdot 10^{-2}$	43,194	4.571	0.1811	−19.65
50	$1 \cdot 10^{-2}$	58,280	4.565	0.1813	−19.59

(a) Grid sensitivity table

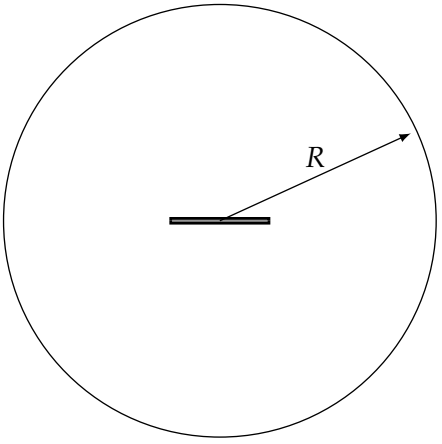

(b) Computational domain

Figure 20: Grid sensitivity of the weakly nonlinear analysis at ($\tilde{m} = 1000, Re = 2682.81$).

reference value obtained at $R = 50$. In any case, it should be kept in mind that these variations of a few percent are negligible in regards to the physical variations observed in fig. 5.

REFERENCES

Amandolèse, Xavier 2016 Low Speed Flutter and Post-Critical Behaviour of Flat Plate and Naca0018 Section Models in a Wind Tunnel. In *First International Symposium on Flutter and its Application*, pp. 447–455.

Amandolese, X., Michelin, S. & Choquel, M. 2013 Low speed flutter and limit cycle oscillations of a two-degree-of-freedom flat plate in a wind tunnel. *Journal of Fluids and Structures* **43**, 244–255.

Badia, Santiago & Codina, Ramon 2007 On some fluid–structure iterative algorithms using pressure segregation methods. Application to aeroelasticity. *International Journal for Numerical Methods in Engineering* **72** (1), 46–71.

Balay, Satish, Abhyankar, Shrirang, Adams, Mark F., Brown, Jed, Brune, Peter, Buschelman, Kris, Dalcin, Lisandro, Dener, Alp, Eijkhout, Victor, Gropp, William D., Karpeyev, Dmitry, Kaushik, Dinesh, Knepley, Matthew G., May, Dave A., McInnes, Lois Curfman, Mills, Richard Tran, Munson, Todd, Rupp, Karl, Sanan, Patrick, Smith, Barry F., Zampini, Stefano, Zhang, Hong & Zhang, Hong 2019 PETSc Web page.

Bendiksen, Oddvar O. 2011 Review of unsteady transonic aerodynamics: Theory and applications. *Progress in Aerospace Sciences* **47** (2), 135–167.

Bhat, Shantanu S. & Govardhan, Raghuraman N. 2013 Stall flutter of NACA 0012 airfoil at low Reynolds numbers. *Journal of Fluids and Structures* **41**, 166–174.

Bisplinghoff, Raymond L., Ashley, Holt & Halfman, Robert L. 1955 *Aeroelasticity*.

Coller, B.D. & Chamara, P.A. 2004 Structural non-linearities and the nature of the classic flutter instability. *Journal of Sound and Vibration* **277** (4-5), 711–739.

Dimitriadis, Grigorios 2017 *Introduction To Nonlinear Aeroelasticity*. John Wiley & Sons, Ltd.

Dimitriadis, Grigorios & Li, Jing 2009 Bifurcation Behavior of Airfoil Undergoing Stall Flutter Oscillations in Low-Speed Wind Tunnel. *AIAA Journal* **47** (11), 2577–2596.

Gallaire, Francois, Boujo, Edouard, Mantic-Lugo, Vladislav, Arratia, Cristobal, Thiria, Benjamin & Meliga, Philippe 2016 Pushing amplitude equations far from threshold: Application to the supercritical Hopf bifurcation in the cylinder wake. *Fluid Dynamics Research* **48** (6), 1–12.

Gianetti, Flavio & Luchini, Paolo 2007 Structural sensitivity of the first instability of the cylinder wake. *Journal of Fluid Mechanics* **581**, 167–197.

Guermond, J. L., Minev, P. & Shen, Jie 2006 An overview of projection methods for incompressible flows. *Computer Methods in Applied Mechanics and Engineering* **195** (44-47), 6011–6045.

Hecht, F 2012 New development in FreeFem++. *J. Numer. Math.* **20** (3-4), 251–265.

Hourigan, K., Thompson, M.C. & Tan, B.T. 2001 Self-sustained oscillations in flows around long blunt plates. *Journal of Fluids and Structures* **15** (3-4), 387–398.

Huerre, Patrick & Monkewitz, Peter A 1990 Local and global instabilities in spatially developing flows. *Annual review of fluid mechanics* **22** (1), 473–537.

Jallas, Damien, Marquet, Olivier & Fabre, David 2017 Linear and nonlinear perturbation analysis of the symmetry breaking in time-periodic propulsive wakes. *Physical Review E* **95** (6), 1–15.

Lee, B. H. K. & Jiang, L.Y. 1999 Flutter of an Airfoil With a Cubic Restoring Force. *Journal of Fluids and Structures* **13**, 75–101.

Marquet, Olivier & Lesshafft, Lutz 2015 Identifying the active flow regions that drive linear and nonlinear instabilities .

Meliga, Philippe, Gallaire, François & Chomaz, Jean-Marc 2012 A weakly nonlinear mechanism for mode selection in swirling jets. *Journal of Fluid Mechanics* **699**, 216–262.

Menon, Karthik & Mittal, Rajat 2019 Flow physics and dynamics of flow-induced pitch oscillations of an airfoil. *Journal of Fluid Mechanics* **877**, 582–613.

Nayfeh, Ali Hasan & Balachandran, Balakumar. 1995 *Applied nonlinear dynamics : analytical, computational, and experimental methods*. Wiley.

Padmanabhan, Madhusudan A., Dowell, Earl H. & Pasiliao, Crystal L. 2018 Computational Study of Aeroelastic Limit Cycles due to Localized Structural Nonlinearities. *Journal of Aircraft* **55** (4), 1531–1541.

Paladini, Edoardo, Marquet, Olivier, Sipp, Denis, Robinet, Jean Christophe & Dandois, Julien 2019 Various approaches to determine active regions in an unstable global mode: Application to transonic buffet. *Journal of Fluid Mechanics* **881** (M), 617–647.

Petot D 1989 Modélisation du décrochage dynamique par équations différentielles. *La Recherche aérospatiale* .

Razak, Norizham Abdul, Andrianne, Thomas & Dimitriadis, Grigorios 2011 Flutter and Stall Flutter of a Rectangular Wing in a Wind Tunnel. *AIAA Journal* **49** (10), 2258–2271.

Schewe, G., Mai, H. & Dietz, G. 2003 Nonlinear effects in transonic flutter with emphasis on manifestations of limit cycle oscillations. *Journal of Fluids and Structures* **18** (1), 3–22.

Shaabani-Ardali, Léopold, Sipp, Denis & Lesshafft, Lutz 2019 Vortex pairing in jets as a global Floquet instability: modal and transient dynamics. *Journal of Fluid Mechanics* **862**, 951–989.

Šidlof, Petr, Vlček, Václav & Štěpán, Martin 2016 Experimental investigation of flow-induced vibration of a pitch–plunge NACA 0015 airfoil under deep dynamic stall. *Journal of Fluids and Structures* **67**, 48–59.

Stanford, Bret & Beran, Philip 2013 Direct flutter and limit cycle computations of highly flexible wings for efficient analysis and optimization. *Journal of Fluids and Structures* **36**, 111–123.

Tang, Deman & Dowell, Earl H. 2002 Limit-Cycle Hysteresis Response for a High-Aspect-Ratio Wing Model. *Journal of Aircraft* **39** (5), 885–888.

Theodorsen, Theodore 1935 General Theory of Aerodynamic Instability and the Mechanism of Flutter. *Tech. Rep.*. NACA Report 496, Langley.

Thomas, J. P., Dowell, E. H. & Hall, K. C. 2002 Nonlinear inviscid aerodynamic effects on transonic divergence, flutter and limit cycle oscillations. *AIAA Journal* **40** (4), 638–646.

Thomas, J P, Dowell, E H & Hall, K C 2004 Modeling viscous transonic limit-cycle oscillation behavior using a harmonic balance approach. *Journal of Aircraft* **41** (6), 1266–1274.

Van Rooij, A. C. L. M., Nitzsche, J. & Dwight, R. P. 2017 Prediction of Aeroelastic Limit-Cycle Oscillations Based on Harmonic Forced-Motion Oscillations. *AIAA Journal* **55** (10), 3517–3529.

Woolston, Donald S, Runyan, Harry L. & Andrews, Robert E. 1957 An Investigation of Effects of Certain Types of Structural Nonlinearities on Wing and Control Surface Flutter. *Journal of the Aeronautical Sciences (Institute of the Aeronautical Sciences)* **24** (1), 57–63.

Woolston, Donald S., Runyan, Harry L. & Byrdsong, Thomas A. 1955 Some Effects of System Nonlinearities in the Problem of Aircraft Flutter. *Tech. Rep.*. NACA.